

# Quantifying the Impact of Modeling Fidelity on Different Substructure Concepts - Part II: Code-to-Code Comparison in Realistic Environmental Conditions

Francesco Papi<sup>1</sup>, Giancarlo Troise<sup>2</sup>, Robert Behrens de Luna<sup>3</sup>, Joseph Saverin<sup>3</sup>, Sebastian Perez-Becker<sup>3</sup>, David Marten<sup>3</sup>, Marie-Laure Ducasse<sup>4</sup>, Alessandro Bianchini<sup>1</sup>

<sup>1</sup>Department of Industrial Engineering, University of Florence, Firenze, 50139, Italy

<sup>2</sup>Seapower srl, Naples, 80121, Italy

<sup>3</sup>Hermann Föttinger Institute, Technical University of Berlin, Berlin, 10623, Germany

<sup>4</sup>Saipem S.A., 1/7 Avenue San Fernando, 78884 Saint Quentin Yvelines cedex, France

Correspondence to: A. Bianchini ([alessandro.bianchini@unifi.it](mailto:alessandro.bianchini@unifi.it)) or F. Papi ([fr.papi@unifi.it](mailto:fr.papi@unifi.it))

**Abstract.** Consensus is arising on considering floating offshore wind as the most promising technology to increase renewable energy generation offshore. While evolving quickly from a technological point of view, Floating Offshore Wind Turbines (FOWTs) are challenging, as their performance and loads are governed by complex dynamics that are a result of the coupled influence of wind, waves, and currents on the structures. Many open challenges therefore still exist, especially from a modeling perspective. This study contributes to the understanding of the impact of modeling differences on FOWT loads by comparing three FOWT simulation codes, QBlade-Ocean, OpenFAST, and DeepLines Wind<sup>®</sup> and three substructure designs, a semi-submersible, a spar-buoy, and the two-part concept Hexafloat in realistic environmental conditions. This extensive comparison represents one of the main outcomes of the H2020 project FLOATECH. In accordance with international standards for FOWT certification, multiple design situations are compared, including operation in normal power production and parked conditions. Results show that the compared codes agree well in the prediction of the system dynamics, regardless of the fidelity of the underlying modeling theories. Some differences between the codes emerged however in the analysis of fatigue loads, where, contrary to extreme loads, specific trends can be noted. With respect to QBlade-Ocean, OpenFAST was found to overestimate lifetime damage equivalent loads up to 14%. DeepLines Wind<sup>®</sup>, on the other hand, underestimated lifetime fatigue loads by up to 13.5%. Regardless of the model and FOWT design however, differences in fatigue loads are larger for tower base loads than for blade root loads, due to the larger influence substructure dynamics have on these loads.

## 1 Introduction

In recent years industrial and academic interest around floating offshore wind energy has been increasing, thanks to its promise to foster wind energy harvesting in offshore areas previously inaccessible with bottom-fixed wind turbines. To fully exploit the advantages of this technology, ever larger and more flexible offshore turbines are being developed and deployed. These systems are challenging to model, as their dynamics are governed by the coupled influence of aerodynamics, hydrodynamics, control, and moorings. As an additional complexity, with large and flexible turbine rotors, aeroelastic coupling also plays an important

32 role. Many of the industry’s work-horse simulation codes have been developed with smaller, more rigid, bottom-fixed rotors in  
33 mind and rely on engineering models, sometimes empirically derived, to model the relevant physical phenomena. In this context,  
34 a real need for verification and validation of these tools exists. Several efforts, past and present, have been put into verification  
35 and validation of offshore simulation codes. Notable examples being the Offshore Code Comparison (“OC” in short) programs  
36 promoted by the International Energy Agency (IEA), OC3, OC4, OC5 and the on-going OC6 (Jonkman and Musial, 2010;  
37 Robertson et al., 2014b, 2017; Bergua and et. al., 2023). Throughout the OC- projects, offshore codes have been compared  
38 against other codes, and against wave-tank experiments. Especially OC4 and OC5 have helped highlight deficiencies in low-  
39 frequency hydrodynamic modeling of semi-submersible type platforms (Robertson et al., 2017) that have allowed the advance  
40 of the state-of-the art in OC6 (Robertson et al., 2020; Wang et al., 2022). Most of these campaigns have found that even simplified  
41 engineering tools are generally able to capture the aerodynamics of these systems well - at times better than expected, such as in  
42 (Bergua and et. al., 2023) – when compared to higher-fidelity and more physically complete aerodynamic models. Throughout  
43 these comparison studies however, a limited number of often simplified inflow conditions have been tested. On the other hand,  
44 some authors have found some differences between modeling theories when the coupled system dynamics are put to the test. In  
45 particular, Corniglion (2022) found increased blade root fatigue loads when comparing Blade Element Momentum Theory  
46 (BEMT) to a higher fidelity Lifting-Line Free Vortex Wake (LLFVW) method. Similar considerations were also drawn by other  
47 authors such as (Boorsma et al., 2020; Perez-Becker et al., 2020) when comparing fatigue load predictions on onshore wind  
48 turbines. In detail, Boorsma et al. (Boorsma et al., 2020) have linked the increase in fatigue loads to increased 1P load variation,  
49 while Perez-Becker et al. (Perez-Becker et al., 2020) have found that even small differences in aerodynamic modeling can lead  
50 to different controller reactions, influencing overall loading and highlighting the importance of accurately modeling the entire  
51 coupled dynamics of the system. In the case of FOWTs, dynamics are even more complex as the turbine moves in response and  
52 in reaction to the incoming wind and wave variations. This introduces additional inertial and gravitational loading on many  
53 structural components (Jonkman and Matha, 2011). Thus, differences in rotor loading may influence the response of the system,  
54 indirectly influencing other component loads and amplifying the differences between the models.

55 The current study contributes to the field by presenting the outcomes of an extensive code-to-code comparison considering  
56 realistic environmental conditions and three different floating substructure designs. Environmental conditions from an existing  
57 European site are obtained using the procedure described in (Papi et al., 2022c) to obtain realistic distributions of wind speed,  
58 significant wave height, peak spectral period and wind-wave misalignment. The three test-cases - a spar-buoy, a semi-  
59 submersible and the innovative two-part floater concept; Hexafloat, recently proposed by Saipem - are simulated in a variety of  
60 Design Load Cases (DLCs), including both power-production and parked conditions, as well as wind gusts. The test-cases are  
61 simulated using three offshore codes, OpenFAST, DeepLines Wind and QBlade-Ocean, which was recently extended to enable  
62 offshore simulations within the Horizon 2020 project FLOATECH. The latter code includes higher-fidelity modeling features  
63 such as LLFVW wake aerodynamics and explicit buoyancy calculation, as illustrated in (Behrens De Luna et al., 2023).

64 The predicted dynamics are compared in terms of extreme loads, fatigue loads and statistics. Time series are also compared in  
65 detail to give more insight into the differences in dynamics. The entire input conditions and compared datasets are available  
66 open-access and can act as validation databases for other offshore codes or as a benchmark for future modeling improvements.  
67 An extensive comparison, involving three different models with different substructure designs, three different numerical codes  
68 and multiple DLCs that include hundreds of simulations is an important point of novelty of this study and does not come without  
69 challenges. In fact, comparing coupled simulations that are aero-hydro-servo-elastic in nature such as in this study makes  
70 isolating the potential sources of any differences challenging. Nonetheless, it offers the unique opportunity of evaluating the  
71 trade-off between computational time and accuracy of the modeling theories in terms of their impact on the final design load  
72 predictions in a realistic scenario. It also allows one to highlight user-bias in the set-up of FOWT simulations. In this view, some  
73 critical aspects to consider during model set-up, that lead to significant differences in ultimate and fatigue loads in the compared  
74 models such as structural damping ratios and control strategy are discussed in detail.

75 This paper is organized as follows: In Sect. 2 the procedure required to set up the code-to-code comparison that is presented  
76 herein is detailed, starting from environmental conditions and continuing with DLC definition, test-case selection, and data post-  
77 processing. In Sect. 3 some details regarding the modeling theories underpinning the compared tools are given. In Sect. 4 the  
78 main results are presented, starting from a general statistical comparison of key metrics, and then moving to the comparison of  
79 design-driving extreme and fatigue loads. The principal results are discussed, and the conclusions drawn in Sect.5

## 80 **2 A Procedure for Code-to-Code Comparison of FOWTs in Realistic Environmental Conditions**

81 The set-up of a design load calculation of a FOWT is a complex task on its own. Expertise is required in the selection and set-  
82 up of relevant DLCs in compliance with the various international standards (International Electrotechnical Commission, 2019;  
83 DNVGL, 2016). In the case of FOWTs, expertise is also required in the selection of environmental conditions to use, which are  
84 site dependent. Finally, a full load calculation can produce thousands of hours of time series data, and data processing techniques  
85 are required to make it more manageable and useful for the design process. In the context of this study, all these aspects will be  
86 briefly presented as they have already been touched upon in two publications by the authors (Papi et al., 2022c; Papi and  
87 Bianchini, 2023), that will be referenced later on in this Section where appropriate.

### 88 **2.1 European Met-Ocean Conditions**

89 Design classes are not currently prescribed for any type of offshore wind turbine as they are for onshore wind turbines, in favor  
90 of standardization. Although the need for such standardization is acknowledged and encouraged in the DNVGL-SST-0119  
91 design standard (DNVGL, 2018), the designer is currently required to verify the turbine and substructure combination of choice  
92 for specific installation sites. As discussed in the following Sections, standards require the definition of specific wind conditions,  
93 normally grouped in “models” such as the Normal Turbulence Model (NTM), and sea condition, generally grouped in “sea  
94 states”. Some databases containing such met-ocean data can be found in previous work – for a comprehensive literature review

95 see (Papi and Bianchini, 2023) – however if we restrict our research to Europe, we did not find suitable met-ocean conditions  
96 for this analysis. Therefore, an open-source procedure to obtain and prepare long-term environmental data so it can be used in a  
97 design load calculation of an offshore wind turbine was developed. The procedure that is detailed in (Papi et al., 2022c) and is  
98 available open-access for others to use and improve upon (10.5281/zenodo.6972014).

99 Data is obtained from the Copernicus re-analysis database ERA5. Environmental data is available on a 30x30 km grid, therefore  
100 the procedure can be applied to a generic world-wide offshore site. In this study, hourly records of wind speed, wind direction,  
101 significant wave height, wave direction and peak spectral period from 1979 to 2000 for a site located west of the Scottish island  
102 of Barra are used. This location was chosen because of its particularly harsh environment, expected to increase non-linearities  
103 and differences in the examined models, and because it is also used in other EU-funded projects such as LifeS50+ (Antonia  
104 Krieger et al., 2015) and CoreWind (Vigara et al., 2020). Although more research would be needed to properly support this  
105 claim, due to the severity of the considered met-ocean conditions, it is reasonable to believe that any differences between the  
106 codes represent an upper limit, and smaller differences are likely to be found in less demanding conditions.

107 The open-source Python tool Virocon (Haselsteiner et al., 2019) is leveraged to build a joint probabilistic model of the dataset,  
108 able to describe the long-term probability of the four environmental variables that are considered: wind speed ( $U_w$ ), significant  
109 wave height ( $H_S$ ), peak spectral period ( $T_p$ ) and wind-wave misalignment ( $M_{ww}$ ). The model is then used to find the most likely  
110 combination of  $H_S$  and  $T_p$  for a given  $U_w$ , defining the Normal Sea State (NSS), and to define environmental contours: extreme  
111 conditions with 50-year recurrence period that are used to define the Extreme Sea State (ESS) and the Severe Sea State (SSS).  
112 More details on how these sea states are defined are summarized in (Papi et al., 2022c), while information on environmental  
113 contours and their applications to offshore wind turbines can be found in (Haselsteiner et al., 2020, 2021; Valamanesh et al.,  
114 2015).

## 115 **2.2 DLC Selection and Simulation Conditions**

116 Code-to-code comparisons in a variety of environmental conditions are performed in this study. As such, simulations in various  
117 met-ocean conditions are performed. The specific combination of met-ocean condition and operating condition is a Design Load  
118 Case (DLC). In this study normal operating conditions and parked DLCs are simulated, as shown in Table 1. , While this  
119 paragraph contains a general overview of the selected DLCs, a more detailed explanation of the selected process can be found  
120 in the FLOATECH project deliverables (Papi et al., 2022a, b), and in (Papi and Bianchini, 2023). To obtain representative  
121 ultimate loads, operation in extreme turbulence (DLC 1.3), in severe seas (DLC 1.6) and during an extreme operating gust with  
122 direction change (DLC 1.4) are considered. In these load cases, wind and waves are considered aligned as a worst case scenario,  
123 in compliance with international standard prescriptions (IEC TS 61400-3-2:2019 | IEC Webstore, 2023). In DLCs where the  
124 turbine is parked during one year (DLC 6.3) and fifty years extreme environmental conditions, with (DLC 6.2) and without  
125 (DLC 6.1) grid loss, a  $\mp 30^\circ$  wind-wave misalignment is also considered. All ultimate load DLCs simulations are one hour long,  
126 with the exception of DLC 1.4, where simulations are 10 minutes long. In this DLC, interest is put on the extreme loads caused  
127 by the transient wind gust. As such, these simulations can be shortened without loss of relevant information. Moreover, multiple

128 turbulent seeds and yaw misalignments are considered within each DLC. For fatigue loads, normal operation in normal inflow  
 129 and sea conditions (DLC 1.2) is considered. In this DLC, in accordance with indications coming from design standards  
 130 (International Electrotechnical Commission, 2019), that require the full design space to be explored, multiple sea states are  
 131 examined, including multiple combinations of the four environmental variables. Therefore, the design space is divided into bins,  
 132 and at least one model evaluation for each bin is required. To keep the number of simulations manageable in the context of a  
 133 code-to-code comparison endeavor, two strategies to reduce the number of required model evaluations are adopted. Both  
 134 strategies were proposed in (Stewart, 2016); the first is the “probability sorting method”, where the least likely bins are discarded  
 135 as these conditions are unlikely and are expected to have little impact on fatigue loads. In this study the most likely bins, ensuring  
 136 a total combined probability of 90% are kept in the analysis. The second strategy is bin coarsening, in which the width of the  
 137 bins is increased, thereby reducing their number. As discussed in (Papi and Bianchini, 2023), by combining the two strategies a  
 138 relatively manageable number of bins is obtained: 252. For each bin two half-hour simulations are performed with different yaw  
 139 misalignments.

140

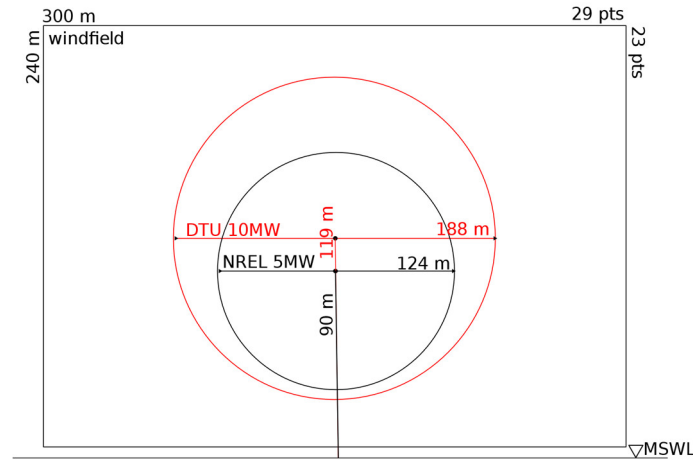
141 **Table 1: DLCs used in this study. Normal operating conditions in various sea states and turbulence levels in DLCs 1.2 to 1.6 for the**  
 142 **evaluation of fatigue (F) and ultimate (U) loads. In DLCs 6.1 to 6.3 the FOWTs are parked in extreme conditions. In DLC 6.2 a grid**  
 143 **loss scenario is modelled, and thus multiple values of yaw-error are considered. Acronyms are described in nomenclature list.**

DLC	wind		waves				dur. [s]	seeds/ws	yaw	n° ws	sims	type
	model	speed	model	height	period	dir.						
1.2	NTM	$V_{in}-V_{out}$	NSS	-	-	MUL	1800	1	0, 10°	11	504	F
1.3	ETM	$V_{in}-V_{out}$	NSS	$E[H_S V_{hub}]$	$E[T_P H_S]$	COD	1800	9	0, $\mp$ 10	11	99	U
1.4	ECD	$V_r \mp 2$ m/s	NSS	$E[H_S V_{hub}]$	$E[T_P H_S]$	COD	600	-	0	6	12	U
1.6	NTM	$V_{in}-V_{out}$	SSS	$H_S$ , SSS	$E[T_P H_S]$	COD	3600	9	0, $\mp$ 10	11	99	U
6.1	EWM50	$V_{50}$	ESS	$H_{S50}$	$E[T_P H_S]$	0°, $\mp$ 30°	3600	2	0, $\mp$ 10	1	12	U
6.2	EWM50	$V_{50}$	ESS	$H_{S50}$	$E[T_P H_S]$	0°, $\mp$ 30°	3600	2	0,45,90 135,180	6	12	U
6.3	EWM1	$V_1$	ESS	$H_{S1}$	$E[T_P H_S]$	0°, 30°	3600	2	0, $\mp$ 20	1	12	U

144

145 To ensure a fair comparison between the codes an attempt was made to match environmental inputs as well as possible in the  
 146 numerical models. The wave time series are generated in DeepLines and then imported in OpenFAST and QBlade, while the  
 147 wind fields are generated by each participating institution using the same TurbSim (Jonkman, 2014) settings. The same wind  
 148 fields are used in all three test cases, as if they were installed in the same site, regardless of the rotor size used. Therefore, the  
 149 larger 10MW rotor defines the overall size of the wind field. A schematic representation of the wind fields is shown in Fig. 1.

150

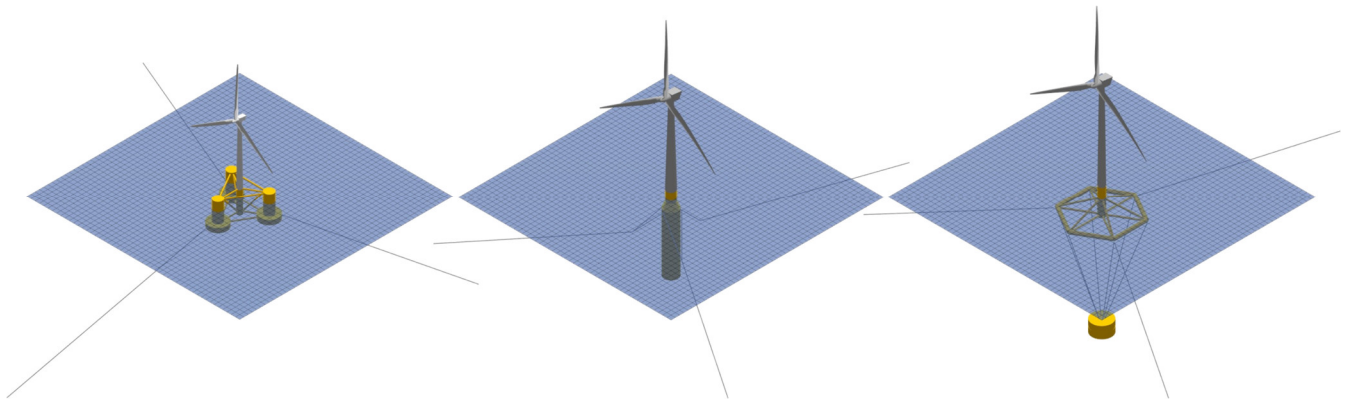


151

152 **Figure 1: Schematic illustration of the wind field dimensions as used in this study with respect to the NREL 5MW and DTU 10MW**  
 153 **rotors. The same wind fields are used on all three test-cases regardless of rotor size.**

### 154 2.3 Considered FOWT Designs

155 For the sake of generality and completeness of the analysis three floating turbine concepts are analyzed. Each test case features  
 156 a different floating platform concept, namely a semi-submersible, a spar-buoy and Hexafloat. The three concepts are all derived  
 157 from those in (Perez-Becker et al., 2022; Behrens De Luna et al., 2023), where some calibration was required to properly align  
 158 the models with the experiments. The main characteristics of the three test-cases are detailed in the following.



159

160 **Figure 2: Illustration of the examined numerical models in QBlade-Ocean. From left to right: NREL 5MW OC4, DTU 10MW Softwind**  
 161 **and DTU 10MW Hexafloat.**

162

#### 163 2.3.1 NREL 5MW OC4 DeepCwind

164 The NREL 5MW OC4 semi-submersible FOWT (hereafter OC4) is an open-access turbine model defined in (Robertson et al.,  
 165 2014a), upon which many code-to-code comparison exercises are based (Robertson et al., 2014b, 2017). It makes use of the

166 NREL 5MW RWT rotor (Jonkman et al., 2009), representative of a utility-scale multi-MW rotor. The rotor is mounted on the  
167 DeepCwind semisubmersible floating platform. The platform was developed with the aim of generating test data for use in the  
168 validation of FOWT modeling tools.

169 The same tower design that was developed for use on the OC3-Hywind spar platform (Jonkman, 2010) is used. The semi-  
170 submersible floater consists of a main central column connected to the tower and three side columns spaced 120° apart. The  
171 offset columns are larger at the base, acting like heave plates to control the vertical motion of the FOWT and are connected  
172 together through a series of braces. A catenary mooring system is used. Three 120° lines are used to anchor the turbine to the  
173 seabed with one mooring line pointing directly upwind and the other two downwind.

### 174 **2.3.2 DTU 10MW Softwind**

175 The DTU 10 MW Softwind spar FOWT (hereafter Softwind) is a 1:40 scale floating platform designed by École Centrale de  
176 Nantes to develop, demonstrate, and validate a Software in the Loop (SiL) approach whereby an actuator is used to simulate the  
177 aerodynamic forcing at model scale in place of a scaled rotor. The model and experiments are described in (Arnal, 2020). The  
178 rotor nacelle assembly (RNA) is described in (Bak et al., 2013). With respect to the models used in (Behrens De Luna et al.,  
179 2023) that mimic the characteristics of the experiments (Arnal, 2020), some changes were implemented to increase the robustness  
180 of the numerical simulations when using the realistic met-ocean conditions considered in this work. Namely, the tower was  
181 stiffened, moving to a stiff-stiff design to avoid wave and 3P tower resonance. The tower designed by Olav-Olsen<sup>1</sup> in the  
182 LifeS50+ project for the OO-Star floater is used (Borg, 2015; Yu, n.d.). Notably this tower is heavier than the one used in the  
183 Softwind test campaign. The mass distribution in the floater is also changed. In order to have a realistic mass distribution and  
184 inertial properties, we hypothesized the use of high-density ballast in the spar body, thus lowering the Center of Gravity (CoG)  
185 with respect to the scaled model used in the experiments, which housed control electronics and batteries within the buoy. The  
186 mass of the floater is also lowered by approximately 2% to compensate for the heavier tower and maintain approximately the  
187 same draft. Furthermore, lowering the CoG lowers the platform pitch natural period, allowing for the use of a faster controller,  
188 as explained in Sect. 3.3. The specific changes are detailed in (Papi et al., 2022a). This modified floater design is not intended  
189 to be built and is only meant for numerical comparisons using a realistic design that is also numerically stable. These changes  
190 are therefore deemed appropriate for the goal of this study.

191 In DeepLines, after unsuccessful initial attempts to align the model to QBlade and OpenFAST, and, in an initial phase, to the  
192 Softwind experiments (Arnal, 2020), a different tuning approach was employed for the hydrodynamics of the model. In  
193 particular, the pitch and roll inertias of the floater were decreased to better align the respective natural frequencies in free decay  
194 tests, and additional added mass on the spar buoy was introduced through Morison's equation to improve the agreement during

---

<sup>1</sup> The OO-Star Wind Floater has been developed by Dr. Techn. Olav Olsen (OO) since 2010 and is the property OpenFAST Floating Wind Solutions AS. OO has approved that the public model from LifeS50+ can be used for the research activities within FLOATECH. The model shall not be used for other purposes unless it is explicitly approved by OO.

195 surge free-decay tests. Lastly, mooring line tension was lowered to better align with the experimental data. A full description of  
 196 the differences can be found in (Papi et al., 2023).

### 197 **2.3.3 DTU 10MW Hexafloat**

198 The DTU 10MW Hexafloat FOWT (Hereafter Hexafloat) consists of the DTU 10MW RWT mounted to the Hexafloat floater  
 199 concept proposed by Saipem. As shown in Fig. 2, the substructure consists of a floater made of relatively slender steel braces  
 200 connected to a counterweight by six tendons. This floater configuration did not require changes to the tower design and therefore  
 201 the standard onshore tower of the DTU 10MW RWT (Bak et al., 2013) is used. This model is in effect identical to the one used  
 202 and described in (Perez-Becker et al., 2022; Behrens De Luna et al., 2023)

## 203 **2.4 Post-Processing and Data Management**

204 The raw time series data obtained for the three models is post-processed using open-source tools, namely MLife (Hayman, 2012)  
 205 and MExtremes (Buhl, 2015) developed by NREL. The main sensors that are compared in the study are shown in Tab. 1 and  
 206 consist of blade root and tower base bending moments, mooring line fairlead tensions, nacelle fore-aft acceleration, control  
 207 signals and platform motions. Some of these sensors act like a proxy to compare the influence of various physical phenomena  
 208 on loads, such as nacelle acceleration that is used to gauge inertial loads on the tower and platform pitch that is used as indication  
 209 of gravitational tower loading. The mechanisms that relate platform motions and substructure loading are discussed in (Robertson  
 210 and Jonkman, 2011; Papi and Bianchini, 2022) and will only briefly be explained throughout this work where necessary.

211 MLife is used to compute Damage Equivalent Loads (DELs). DELs are the cyclic load amplitudes that cause the same fatigue  
 212 damage to the structure over a certain number of cycles as the time series of a given load sensor. The Palmgren-Miner linear  
 213 damage accumulation hypothesis is used to derive DELs, which can therefore only be considered representative equivalent loads  
 214 if this hypothesis is valid. In this study zero-mean DELs are considered, and thus the mean of each loading cycle is disregarded.  
 215 1Hz DELs give the equivalent damage during one simulation, while lifetime DELs represent the equivalent damage over the  
 216 entire lifetime of the turbine. They can be conceptually thought of as a combination of 1Hz DELs weighted by their respective  
 217 probability of occurrence, which in this case is a distribution that depends on the four environmental variables defined in Sect.  
 218 2.1. As shown in Tab. 1, only the simulations in DCL 1.2 are used to compute DELs.

219 MExtremes is used to compute ultimate loads on the structure. In this case, DLCs 1.3, 1.4, 1.6, 6.1, 6.2 and 6.3 are used. To  
 220 obtain a conservative estimate of ultimate loads in accordance with IEC 61400-1 annex I (International Electrotechnical  
 221 Commission, 2019), an averaging approach is used when computing ultimate loads, as explained in (Buhl, 2015).

222

**Table 1: Sensors considered in the analysis.**

Sensor	OpenFAST ref. sys.	Name	Type
Blade root in-plane/out-of-plane bending moment	Coned CS <b>c</b>	B# Mx / B# My	F/U
Tower base fore-aft/side-side bending moment	Tower base CS <b>t</b>	TB My/TB Mx	F/U



Mooring line fairlead tensions	-	T ML#	F/U
Nacelle fore-aft acceleration	Tower top CS $\mathbf{p}$	Nac. TAx	U
Control signals (blade pitch, gen. torque, rotor speed)	-	$\theta, \tau, \Omega$	-
Platform motions (computed @SWL)	Platform CS	surge, sway, pitch, etc...	-

### 223 3 Methods

224 This work leverages some of the authors' past experience and as such many of the same modeling techniques as described in  
225 (Behrens De Luna et al., 2023) are used, where a more complete description of the employed methods can be found. Three  
226 distinct numerical tools are used in this code-to-code comparison: OpenFAST v3.0, DeepLines Wind<sup>®</sup> and QBlade-Ocean. The  
227 tools have been compared to experimental results on scaled models and have shown, after adequate model tuning, good ability  
228 to capture the behavior of the different systems. The results of this modeling and validation effort are discussed in (Perez-Becker  
229 et al., 2022; Behrens De Luna et al., 2023). The main numerical models in each code are described in this Section.

#### 230 3.1 Aerodynamic Models

231 All the models compared herein use low- to medium-fidelity aerodynamic models. The blade aerodynamics are not explicitly  
232 modeled. Instead, a series of 2D aerodynamic coefficients is used in their place. Corrections to account for 3D flow effects are  
233 built into the aerodynamic coefficients for all the models. Moreover, Gonzalez's variant of the Beddoes-Leishman dynamic stall  
234 model (Leishman, 2016; Damiani and Hayman, 2019) is used in OpenFAST. In QBlade dynamic stall is modeled using Øye's  
235 model (Marten, 2020), while in DeepLines no unsteady airfoil aerodynamics are accounted for. The relative velocities acting  
236 on the blades are determined by the wake model. A Dynamic Blade Element Momentum (DBEM) wake model is used in  
237 OpenFAST and DeepLines, where the rotor is divided into a series of radial and azimuthal streamtubes and for each streamtube  
238 a momentum balance is performed. More details on BEM models can be found in (Burton, 2001; Hansen, 2008), and details  
239 regarding the specific DBEM model implemented in OpenFAST are in (Ning et al., 2015; Branlard et al., 2022). These models  
240 have been the industry workhorse for decades and although very simple, they have been extended in time through the addition  
241 of empirical sub-models and now fully qualify as engineering models. A higher-order Lifting Line Free Vortex Wake (LLFVW)  
242 model is used in QBlade. Here, the wake is modeled as a series of vortex filaments. Wake nodes are advected downstream by  
243 the incoming wind speed and the cumulative induction of all wake filaments. More details on these models and how they are  
244 implemented in QBlade can be found in (Van Garrel, 2003; Marten et al., 2015). The same aerodynamic lift and drag tables are  
245 used in all three codes for both aerodynamic models and correspond to the public definitions of the NREL 5MW and DTU  
246 10MW rotors.

## 247 **3.2 Structural Models**

248 Structural dynamics are modeled with a modal-based linear superposition approach in OpenFAST through the submodule  
249 ElastoDyn. One limitation is that blade torsion is not modeled in ElastoDyn. In QBlade and DeepLines on the other hand, a  
250 higher fidelity finite-element approach is used, whereby the structural dynamics are modeled with a multi-body representation  
251 that uses Euler-Bernoulli beam elements in a co-rotational formulation (Marten, 2020; Le Cunff et al., 2013). Within OpenFAST  
252 a more sophisticated blade structural model exists that is able to account for blade torsion. Nonetheless, it was chosen to use  
253 ElastoDyn in this study for two reasons. The first reason is to speed up the OpenFAST calculations, as ElastoDyn requires less  
254 computational resources to run. The second reason is that by using a simpler structural model in OpenFAST, the impact of this  
255 choice on the global dynamics and loads of the chosen floating systems can be evaluated.

## 256 **3.3 Control**

257 In all three models the ROSCO v2.4.1 open-source controller (Abbas et al., 2022) is used. This controller has been selected as it  
258 is open-source and it includes an automatic tuning toolbox that can be used to determine the proportional and integral gains of  
259 the blade pitch controller in a simple manner (Lenfest et al., 2020). A traditional  $K\omega^2$  law is used for the torque controller below  
260 rated wind speed. Above rated wind speed constant-torque control strategy is used. The pitch controller gains are tuned using  
261 ROSCO controller's automatic pitch-tuning routine based on the OpenFAST models of the two rotors. The controller includes  
262 a nacelle-velocity feedback loop developed especially for FOWTs, with the objective of avoiding negative blade-pitch controller  
263 damping that can occur in the case of FOWTs. However, this feature is not used in this study. The reason for this being that the  
264 feature did not work for the DeepLines models, as the required nacelle velocity sensor was not available as a controller input in  
265 this code. In order to have a fair comparison between all codes, we decided to disable this feature and instead tuned the pitch  
266 controller to have lower PI-feedback terms. The natural frequencies and damping ratios of the pitch controller used for the three  
267 models are shown in Table 2. For all three models the natural frequency of the blade pitch controller is set below the platform  
268 pitch natural frequency, mitigating possible controller-driven system instabilities. Despite this, a certain degree of blade pitch-  
269 induced platform motion is noted, especially in the Softwind test-case, at near-rated wind speeds. The phenomenon impacts  
270 QBlade simulations more than OpenFAST and DeepLines simulations. The reason for this difference is probably linked to slight  
271 differences in the aerodynamic models that cause different controller reactions, as explained in detail in Sect. 4.3.1.

272 In the OC4 model, a peak-shaving minimum pitch saturation schedule is considered. Peak shaving is used to reduce loads near  
273 rated wind speed by imposing a minimum pitch angle as a function of the low pass filtered wind speed at hub height, as explained  
274 in (Abbas et al., 2022). In this model the same settings are used as in the public example that can be found in the ROSCO  
275 repository.

276 In DLC 1.4 shut-downs are performed by overriding the blade pitch controller with a specified pitch to feather maneuver in each  
277 code. The pitch to feather maneuver is initiated 5 seconds after the wind gust peak, as if the controller was reacting to the  
278 detection of an extreme yaw error and the blades are pitched at a speed of 10 °/s. In DeepLines the pitch to feather maneuver is

279 longer in duration due to a setup difference. In fact, a specific pitch rate during a pitch to feather override maneuver cannot be  
 280 specified in DeepLines, which needs a start and end time of the operation. Therefore, depending on the initial blade pitch angle,  
 281 which depends on the coupled simulation and is thus different for each turbulent seed and each code, this can result in different  
 282 pitch rates.

283 **Table 2: Controller natural frequencies and damping ratios for the three test-cases.**

Model	Nat. f ( $\omega$ )	Damping ratio ( $\beta$ )
NREL 5MW OC4	0.2 [rad/s]	1 [-]
DTU 10MW Softwind	0.14 [rad/s]	1 [-]
DTU 10MW Hexafloat	0.114 [rad/s]	1 [-]

### 284 3.4 Hydrodynamics

285 For the OC4 and Softwind designs a Potential flow with Morison Drag (PFMD) approach is used in both OpenFAST and QBlade,  
 286 whereby hydrodynamics are modeled by combining a potential flow solution with quadratic drag computed with Morison’s  
 287 equation (ME). Full difference-frequency Quadratic Transfer Functions (QTFs) are used in both QBlade and OpenFAST in the  
 288 OC4 design. They were computed and provided for this geometry by ECN using NEMOH (Kurnia et al., 2022), a potential flow  
 289 hydrodynamic solver developed by ECN. On the Softwind design, quadratic hydrodynamic excitation forces are included with  
 290 Newman’s approximation (Faltinsen, 1993). The same hydrodynamic coefficients are used for each design in all three models.  
 291 Buoyancy is modeled differently in the three codes: QBlade and DeepLines model this force explicitly. The spar structure is  
 292 divided into a series of cylindrical sections and buoyancy forces are discretely applied. OpenFAST on the other hand models  
 293 buoyancy force as constant term and a linear stiffness matrix to include the contributions of buoyancy to the restoring forces on  
 294 the platform. Moreover, QBlade is able to model Wheeler wave stretching, which may introduce additional non-linear forcing.  
 295 In the Hexafloat model a different approach is used. In fact, the floater is made of relatively slender braces that can be adequately  
 296 modeled with a ME approach (Faltinsen, 1993). The same added mass and drag coefficients in both the axial and transversal  
 297 directions are used in DeepLines and QBlade, and the hydrodynamic forces predicted by the two codes match well (Perez-Becker  
 298 et al., 2022). The improvements implemented in QBlade to capture the slow-drift hydrodynamic forces described in ((Behrens  
 299 De Luna et al., 2023), Sect. 3.4), are not used in this study, and all three models share the same basic hydrodynamic model, with  
 300 the respective differences highlighted in this Section.

## 301 4 Results

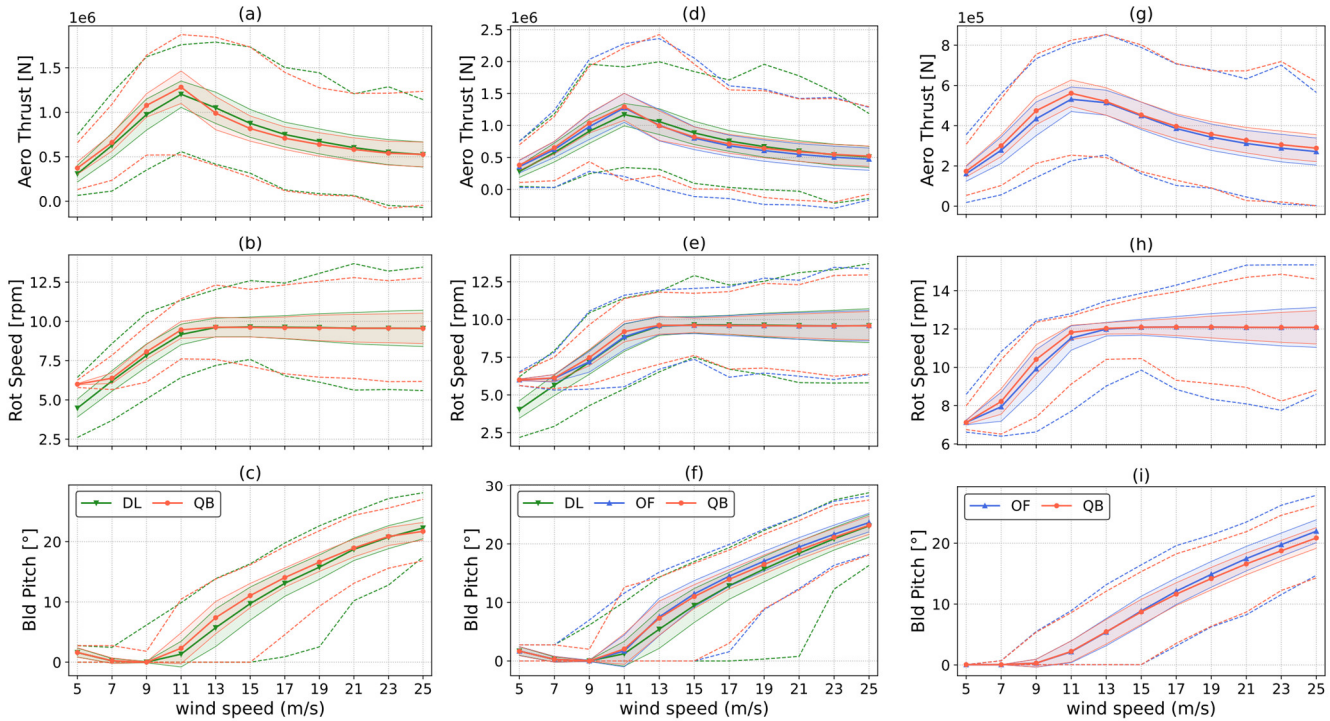
302 In this Section the most relevant results are presented. General statistical information is presented first, followed by a selection  
 303 of ultimate loads recorded in DLCs 1.3 – 6.1 (Table 1) and a selection of lifetime DELs to compare fatigue load predictions. The  
 304 Softwind design is used as the design of choice in most cases as it features all three codes, and results from the other two designs  
 305 are also discussed when necessary. We were unable to complete all the simulations in all three codes in the comparison due to

306 numerical convergence issues. In particular, one out of sixteen simulations in DLC 6.2 in the Softwind model was not completed  
307 in OpenFAST because of instabilities in the structural solver. Moreover, we were unable to complete all simulations in DLCs  
308 1.2 (498/504), 1.3 (86/99), 6.1 (12/18), 6.2 (12/16) and 6.3 (12/18) in DeepLines. Similar issues are also present in the Hexafloat  
309 model in DeepLines, where simulations did not converge in DLCs 1.2 (497/504), 6.1 (12/18), 6.2 (12/16) and 6.3 (12/18). The  
310 cause of the incomplete runs can again be traced back to numerical instabilities in the solution. We chose not to attempt re-  
311 running the simulations with a fine-tuning of the numerical solution scheme parameters because of budget and time constraints  
312 within the project. Therefore, while not an inherent limitation of the code, this result is what could be achieved by a prepared  
313 operator within the project timeline, which is also comparable to that of an industrial project. We were able to complete all the  
314 simulations in QBlade. Results have shown good agreement between the codes in DLCs where the machine is operating, but  
315 some discrepancies when the machine is parked. Moreover, generally larger differences in fatigue loads than in extreme loads  
316 between the codes are noted.

#### 317 **4.1 Statistical Comparison**

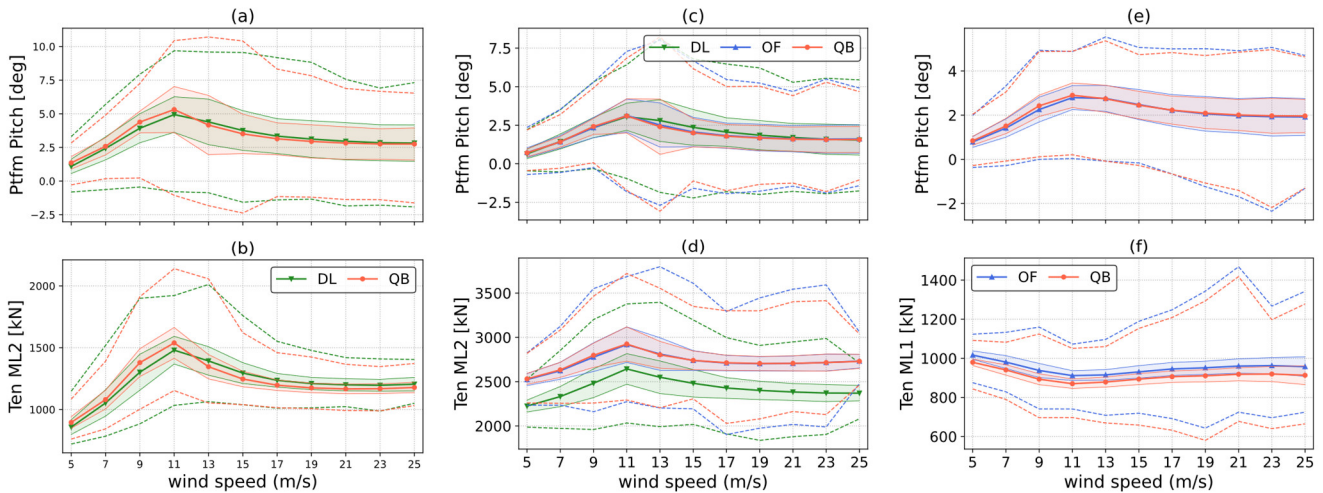
318 Figures 3 and 4 show a statistical comparison of selected operational sensors over the working range of the wind turbines. The  
319 wind speed is extracted at 100 m above mean sea water level. The markers represent the mean values recorded in DLC 1.2, the  
320 shaded area corresponds to twice the standard deviation of the signal for each wind speed and the dashed lines show the minimum  
321 and maximum values recorded during the DLC 1.2 runs. Control sensors, often used to monitor the operation of the wind turbine,  
322 are shown in Fig. 3. Although global trends are the same for all three codes in all three test-cases, some important differences  
323 can be pointed out. With respect to QBlade, mean aerodynamic thrust is lower for DeepLines in the Softwind and Hexafloat test  
324 cases at below rated wind speed and is also lower for OpenFAST in the OC4 test-case. In the case of the OC4 test-case, the  
325 difference in thrust can, at least partially, be attributed to differences in rotor speed (Fig. 3 (h)). In fact, mean rotor speed is  
326 higher in QBlade, causing the rotor to operate at a higher tip speed ratio (TSR), leading to a higher thrust coefficient. Similar  
327 differences in this regard were noted also in previous comparisons between QBlade and OpenFAST (Perez-Becker et al., 2020).  
328 For the Softwind and Hexafloat test-cases (Figs. 3 (b, e)), less difference in rotor speed can be noted, and the difference in thrust  
329 is therefore more likely to be caused solely by differences in the aerodynamic models. The differences in aerodynamic modeling  
330 are also apparent when analyzing blade pitch statistics in Figs. 3 (c, f, i). In fact, while good agreement in mean values can be  
331 noted for QBlade and OpenFAST, mean blade pitch is lower for DeepLines through most of the wind speed range. In addition,  
332 the difference between maximum and minimum blade pitch angles is larger for DeepLines respect to OpenFAST and QBlade.  
333 Moreover, as shown in Fig. 3 (b, e), minimum rotor speed is not enforced in DeepLines, and the rotor operates at lower rpm at  
334 cut-in in both the Hexafloat and Softwind test cases. The ROSCO controller that was used in this code-to-code comparison  
335 required recompiling to be used in DeepLines Wind because the blade pitch and twist angle conventions that are used in this  
336 code differ from those used in QBlade and OpenFAST and as a result, minimum rotor speed is not enforced in DeepLines. To  
337 the best of our knowledge, the controller is functionally identical to that used in OpenFAST and QBlade in all other aspects.  
338 This influences fatigue loads, especially edgewise and in-plane blade root bending moments, that are strongly dependent on

339 cyclic gravitational loading. On the other hand, we can assume the influence of this discrepancy on extreme loads to be limited,  
 340 as these loads are recorded at higher mean wind speeds.



341  
 342 **Figure 3: Statistics of aerodynamic thrust (a, d, g), rotor speed (b, e, h) and blade pitch (c, f, i) as a function of mean wind speed**  
 343 **recorded in DLC 1.2. Solid lines with markers represent mean values, shaded areas represent twice the recorded standard deviation,**  
 344 **dashed lines for the minimum and maximum recorded values. DTU 10MW Hexafloat (a-c), DTU 10MW Softwind (d-f) and NREL**  
 345 **5MW OC4 (g-i).**

346 In Fig. 4, statistics of platform pitch and mooring line tension are shown. For the Softwind and Hexafloat test-case one of the  
 347 two upwind mooring lines is chosen, while for the OC4 test-case the tension of the upwind mooring line is reported in Fig. 4 (f).  
 348 As for the control sensors shown in Fig. 3, good general agreement can be seen for all three codes in all three test-cases. Platform  
 349 pitch is remarkably similar in mean value, standard deviation, and minimum/maximum value for the OC4 test-case (Fig. 4 (e)).  
 350 Very good agreement between OpenFAST and QBlade is also shown in Fig. 4 (a). At 13 m/s mean wind speed however, platform  
 351 pitch standard deviation is higher for QBlade. A similar trend can also be noted in Fig. 4 (c), where again the standard deviation  
 352 of blade pitch is higher for QBlade at 11 m/s and 13 m/s mean wind speeds. Analyzing the time series of the various codes at  
 353 these wind speeds reveals that the increased standard deviation is a result of blade pitch – platform pitch self-excitation. This  
 354 phenomenon is discussed in detail in Sect. 4.3. Mooring line tensions are in good agreement in all three test-cases although some  
 355 differences can be noted. The largest difference is shown in Fig. 4 (b), where a significant difference in mean tension can be  
 356 noted between DeepLines and the other codes. Such difference is a result of different model tuning, as discussed in Sect. 2.3.2.



357

358 **Figure 4: Statistics of platform pitch (a, c, e), upwind mooring line tension (b, f) and tendon tension (d) as a function of mean wind**  
 359 **speed recorded in DLC 1.2. Solid lines with markers represent mean values, shaded areas represent twice the recorded standard**  
 360 **deviation, dashed lines for the minimum and maximum recorded values. DTU 10MW Hexafloat (a-b), DTU 10MW Softwind (c-d) and**  
 361 **NREL 5MW OC4 (e-f).**

362 **4.2 Ultimate Loads**

363 This Section presents the ultimate loads, computed with the maximum averaging method described in Sect. 2.4, for key selected  
 364 load sensors. This Section is focused on understanding which phenomena and modeling differences may influence the prediction  
 365 of extreme loads. The analysis focuses on maximum extreme loads only, disregarding minimum loads to streamline the  
 366 discussion. Minimum extreme loads are reported in Appendix A. In Fig. 5, the ratios of selected ultimate loads on the turbine  
 367 with respect to the values obtained in QBlade, assumed here as benchmark, are shown. The DLCs in which the respective  
 368 maximums are recorded are also reported for each of the bars in Fig. 5. For blade root bending moments, the maximum value  
 369 recorded across the three blades is shown. Figure 5 also reports the blade where the peak load is recorded. Ultimate loads are  
 370 recorded across all the DLCs, thus encompassing both power production and parked load cases, depending on the specific load  
 371 sensor and FOWT design being examined. In the OC4 test case (Fig. 5 (c)) extreme loads are predicted in the same DLC in  
 372 OpenFAST and QBlade, with the exception of blade root in-plane bending moment (BR M<sub>xc</sub>). This FOWT design is the one  
 373 where the best overall agreement between the compared codes was reached. In the Softwind and Hexafloat designs, extreme  
 374 loads are recorded in different DLCs for some load sensors, as is the case for TT F<sub>x</sub> for Softwind and BR M<sub>yc</sub> for Hexafloat. In  
 375 both cases extreme loads predicted across multiple DLCs are very close in magnitude, causing the ultimate extreme load to be  
 376 predicted in different DLCs depending on the specific model's response.

377  
378  
379

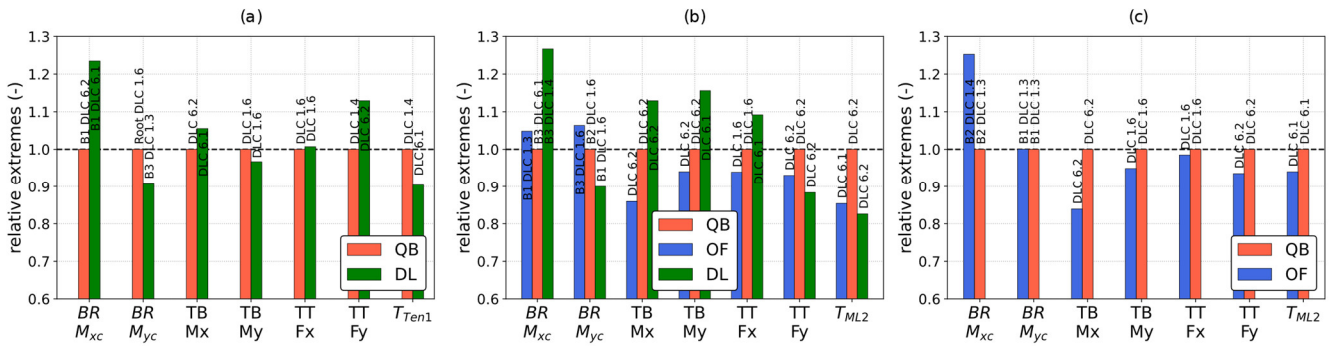


Figure 5: Selection of ultimate loads (maximum) recorded in the three simulation codes. (a) DTU 10MW Hexafloat, (b) DTU 10MW Softwind and (c) NREL 5MW OC4.

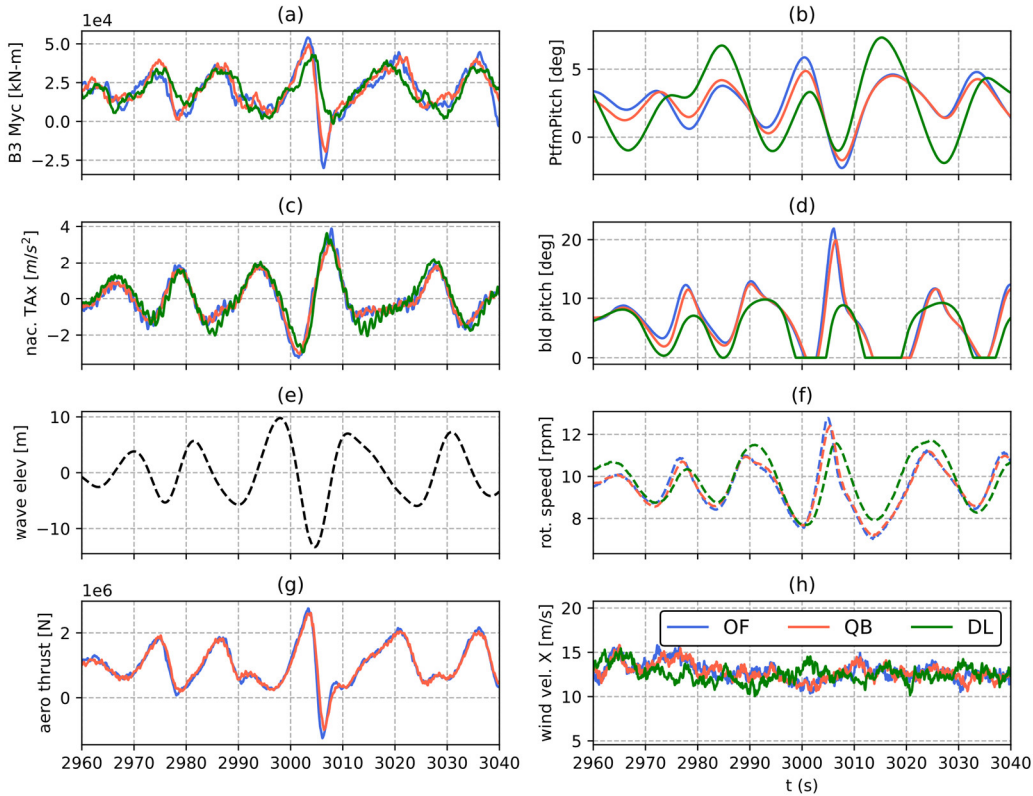


Figure 6: Time series of out-of-plane root bending moment of blade 3 of the Softwind model in DLC 1.6, ( $w_s = 11$  m/s,  $H_s = 9$ ), where maximum bending moment is recorded for OpenFAST. From top to bottom: B#3 out-of-plane root bending moment (a), platform pitch (b), nacelle fore-aft acceleration (c), blade pitch (d), and wave height at platform reference position (e), rotor speed (f), aerodynamic thrust (not available in DeepLines outputs) (g), wind speed at hub height (h).

385

#### 4.2.1 Blade Root Extreme Loads

386

Regarding blade root bending moments, there is larger variation in BR M<sub>xc</sub> ultimate load than BR M<sub>yc</sub>. BR M<sub>yc</sub> is much higher

387

in magnitude than BR M<sub>xc</sub> and thus has a greater influence on component design. Nonetheless, BR M<sub>xc</sub> is approximately 23%

388 higher on the Hexafloat test-case for DeepLines, and 27% higher in the Softwind test-case. Similarly, BR Mxc is approximately  
389 25% higher for OpenFAST in OC4. Out-of-plane blade root bending moments are in better agreement, DeepLines predicting  
390 10% lower loads than QBlade in the Hexafloat and Softwind test-cases, while OpenFAST and QBlade are much closer, the  
391 former being 5% higher in Softwind and nearly identical to QBlade in OC4.

392 The out-of-plane blade root bending moments are mostly influenced by aerodynamic loading, as lift force is directed mostly out-  
393 of-plane. On a FOWT however, the coupled dynamics of the entire system influence these load sensors. This is demonstrated in  
394 Fig. 6, where the time series of multiple load sensors, including BR Myc, platform pitch, aerodynamic thrust and nacelle fore-  
395 aft acceleration are shown at the time instant where the maximum BR Myc in OpenFAST is recorded. When the load peak is  
396 recorded the wind speed is rising and is around the rated wind speed value. In addition, an extreme wave impacts the substructure.  
397 The latter causes the FOWT to move, as shown in the platform pitch and nacelle fore-aft acceleration sensors time series. In turn  
398 this causes large relative inflow variations on the rotor. As hydrodynamic forces cause the platform to swing forward, rotor thrust  
399 increases causing BR Myc to peak. Due to the increase in relative inflow, rotor speed increases (Fig. 6 (d)) and the controller  
400 reacts by aggressively pitching the blades, especially in QBlade and OpenFAST. While controller response depends on and  
401 influences the global response of the system, one reason for the different controller reactions in DeepLines is the different wind  
402 speed in this code (Fig. 6 (e)). In fact, the same wind fields are used in all three codes, but a time-shift is present in DeepLines  
403 with respect to the other models due to differences in how the wind fields are imported. In fact, depending on the simulation  
404 tool, wind fields are often shifted on import in order to make sure that the turbine is fully immersed in the wind field in case of  
405 yaw misalignment. On the other hand, no such shift is present in the wave fields. Therefore, environmental inputs are out of sync  
406 if OpenFAST and QBlade are compared to DeepLines. The increase in blade pitch is able to limit rotor speed overshoot but  
407 causes a sudden decrease in rotor loading, which in turn is the cause of BR Myc reaching a local minimum shortly after peaking.  
408 Therefore, platform motion influences BR Myc indirectly: not through variation in inertial and gravitational loads but through  
409 variation in aerodynamic loading. In summary, even small differences in aspects such as input conditions, hydrodynamics,  
410 aerodynamics, control, and overall set-up definition can influence ultimate loads through different system dynamic behavior.

#### 411 **4.2.2 Tower Base Extreme Loads**

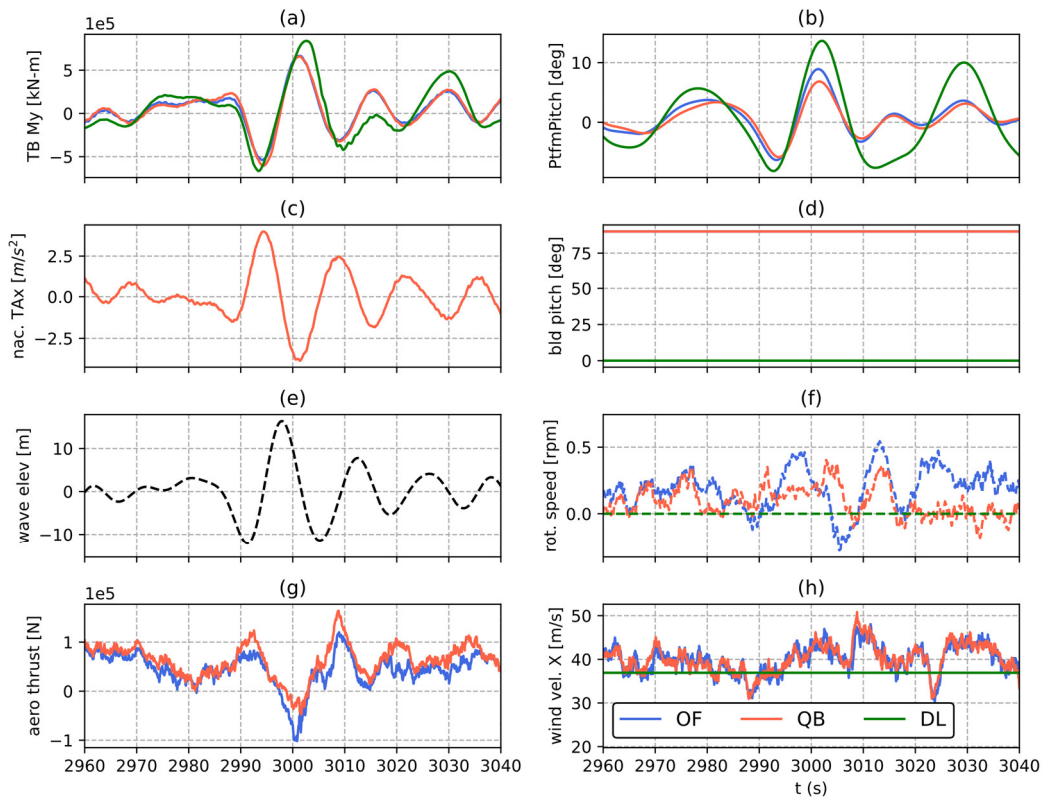
412 Shifting focus to tower base loads, fore-aft (TB My) are, similarly to blade root loads, greater in magnitude than side-side loads  
413 (TB Mx) that will thus be treated briefly. Side-side tower base bending moment (TB Mx) ultimate load always occurs in parked  
414 conditions for all three test-cases and all three design codes. Moreover, except for DeepLines in the Hexafloat test-case, ultimate  
415 loads always occur in DLC 6.2, where in addition to +/- 30° incoming wave heading, yaw misalignment is present.

416 In all three test-cases a strong correlation between platform roll and TB Mx is present, indicating that these ultimate loads are  
417 hydrodynamics-driven. In fact, as the RNA and tower are heavy components, gravitational and inertial loads can be significant  
418 on FOWT towers. Regarding specific test-cases, in OC4 TB Mx ultimate load is approximately 16% lower in OpenFAST. This  
419 discrepancy is mainly caused by response at the tower natural frequency in QBlade, which is not present in OpenFAST. On the  
420 other hand, if time series of TB Mx are compared for the Softwind test-case, little variation can be noted between the three codes.



421 For this load sensor the difference between QBlade and OpenFAST ultimate loads that is shown in Fig. 5, is amplified by the  
 422 maximum averaging technique. As described in Sect. 2.4, the ultimate load in load cases with multiple turbulent seeds  
 423 is computed as the maximum value closest to the mean of the maximums recorded across all the turbulent seeds. Therefore, because  
 424 ultimate loads are slightly different in QBlade and OpenFAST, the peak load closest to the mean is recorded in different seeds  
 425 for the two codes. This demonstrates how small differences between the models can be amplified by the post-processing  
 426 technique.

427 Maximum tower base fore-aft bending moment (TB My) is also recorded in parked conditions in the Softwind test-case - DLC  
 428 6.2 for QBlade and OpenFAST and DLC 6.1 for DeepLines. Analyzing the times series of TB My in DLC 6.1 (Fig. 7) when  
 429 peak load is recorded in DeepLines, the ultimate load is generated by a combination of gravitational and inertial loading resulting  
 430 from platform motion. Higher values of platform pitch are noted in DeepLines, possibly a result of the slacker mooring lines in  
 431 DeepLines, which explain the higher TB My. On the other hand, in the Hexafloat and OC4 test-cases, maximum TB My is found  
 432 in DLC1.6 for all codes (Fig. 5). In both the latter cases OpenFAST and DeepLines are approximately 5% and 3% lower than  
 433 QBlade in this metric. In this case ultimate loads are recorded around rated wind speed, similarly to BR Myc. Differently from  
 434 the latter, which is analyzed in detail in Fig. 6, in the case of TB My, platform motion contributes directly to tower base loading  
 435 as it increases gravitational and inertial forces. Overall, the three codes are close in this metric confirming that all three are able  
 436 to capture the system dynamics in presence of extreme waves to a similar degree.



437

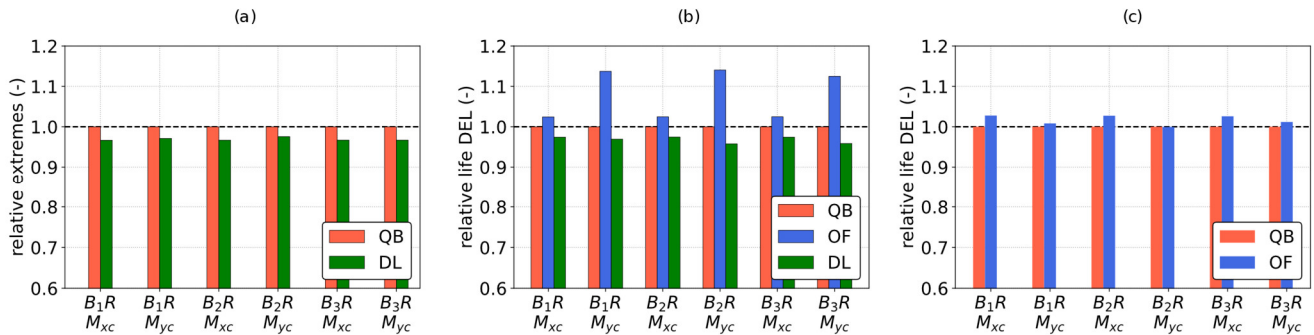
438 **Figure 7: Time series of fore-aft tower base bending moment of the Softwind model in DLC 6.1, ( $w_s = 37$  m/s,  $H_s = 16.5$ ), where**  
 439 **maximum bending moment is recorded for OpenFAST. Tower base fore-aft bending moment (a), platform pitch (b), nacelle fore-aft**  
 440 **acceleration (c), blade pitch (d), and wave height at platform reference position (e), rotor speed (f), aerodynamic thrust (not available**  
 441 **in DeepLines outputs) (g), wind speed at hub height (h).**

442

### 443 4.3 Fatigue Loads

#### 444 4.3.1 Blade Root Fatigue Loads

445 Lifetime, zero-mean DELs computed with the procedure highlighted in Sect. 2.4 at blade root in the coned coordinate system  
 446 are shown in Fig. 8. Contrary to extreme loads, a clear trend is apparent in this case. In fact, with respect to QBlade, Lifetime  
 447 DELs are lower in DeepLines but higher in OpenFAST. In particular, 1Hz DELs are 3-5% lower than QBlade for DeepLines,  
 448 with little variation across the three blades. Indeed, fatigue loads are consistent among the three blades for all three codes and  
 449 all three test-cases, indicating good statistical convergence. Comparing QBlade and OpenFAST, blade root fatigue loads are  
 450 very close (0-3%) in case of the OC4 test-case, while increases of up to 12% in out-of-plane blade root bending moments can be  
 451 seen for Softwind. On the other hand, OpenFAST and QBlade are closer in the prediction of in-plane root bending moments  
 452 than out-of-plane root bending moments. The former are mainly driven by gravity, explaining the smaller differences between  
 453 the compared wind turbine simulation codes.



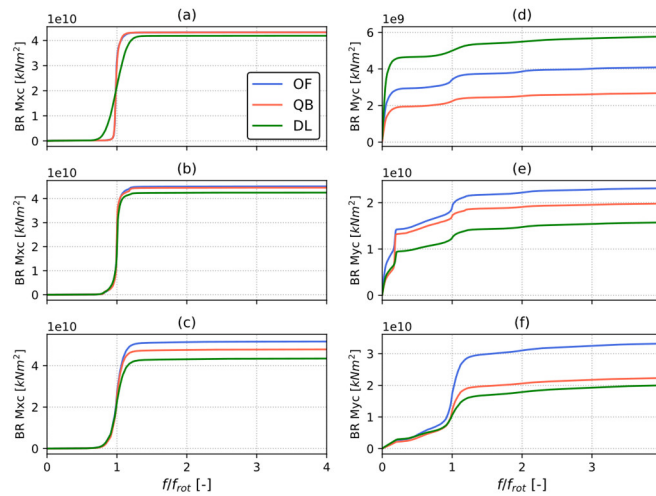
454

455 **Figure 8: Blade root fatigue loads in coned coordinate system: lifetime DELs normalized respect to values computed in QBlade. From**  
 456 **left to right: DTU 10MW Hexafloat, DTU 10MW Softwind and NREL 5MW OC4.**

457 To better understand the differences in Lifetime DELs, the Cumulative Power Spectral Density (CPSD) of blade root bending  
 458 moments for the Softwind FOWT design are shown in Fig. 9. They are obtained as the cumulative sum of the PSD of the signal.  
 459 A CPSD plot is read from left to right; steps in the data indicate peaks in the underlying PSD. When comparing two signals, the  
 460 increase or decrease in distance between the lines indicates the differences between them. The CPSDs for the Hexafloat FOWT  
 461 design look very similar and are not shown here for brevity as similar conclusions can be drawn. At all three of the examined  
 462 wind speeds (7 m/s, 13 m/s and 23 m/s) 1P loads are the main contributors to in-plane fatigue loading (BR M<sub>xc</sub>). The magnitude  
 463 of 1P excitation is lower in DeepLines for all three wind speeds. The most relevant differences in this regard can be seen at 7  
 464 m/s (Fig. 9 (a)) and can be explained by the difference in rotor speed that was noted in Fig. 3. Because minimum rotor speed is

465 not imposed in DeepLines, while it is in QBlade and OpenFAST, the 1P peak spans a larger frequency range in the former and  
466 is lower in magnitude.

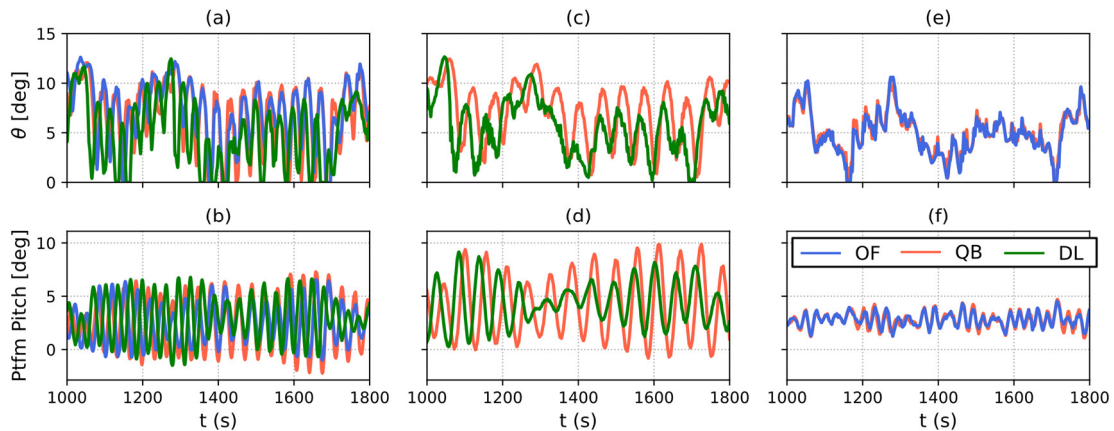
467 Differences are also present in the BR Myc CPSD. The near absence of response between 1P and 2P, at wave frequency, indicates  
468 that apparent wind variations caused by platform motions do not induce relevant fatigue loading for this FOWT design. Three  
469 distinct phenomena drive the differences in this load sensor at the three wind speeds shown in Fig. 9. At 7 m/s (Fig. 9 (d)) wind  
470 speed OpenFAST and DeepLines show higher low-frequency excitation than QBlade. This phenomenon deserves further  
471 attention and will be discussed later in this Section when similar results for the OC4 FOWT design are presented. Moreover,  
472 while small in magnitude when compared to low-frequency response, the 1P peak is larger in OpenFAST. 1P BR Myc load  
473 variation remains larger for OpenFAST across the wind speed range, but are most noticeable at 23 m/s (Figs. 10 (f)).



474  
475 **Figure 9: Cumulative Power Spectral Density (PSD) of blade root in-plane (a-c) and out-of-plane (d-f) bending moment for the**  
476 **Softwind test-case. Frequency is normalized by mean revolution frequency. PSD is computed on all simulations with 7 m/s (a, d), 13**  
477 **m/s (b, e) and 23 m/s (c, f) mean wind speed.**

478 Finally, at 13 m/s the three codes differ mainly in the low-frequency region, where the predicted response in OpenFAST is larger.  
479 Moreover, at this wind speed a large peak at the floater pitch natural frequency can also be seen, especially for QBlade. This  
480 peak in response at the floater natural frequency is caused by blade pitch – floater pitch self-excitation. As described in detail in  
481 (Larsen and Hanson, 2007), on a FOWT an increase in blade pitch causes aerodynamic loads to decrease, and the platform to  
482 swing forward as a consequence. In turn this causes the apparent wind speed on the rotor to increase and rotor speed to follow.  
483 The controller will thus react to the increased rotor speed by increasing blade pitch even further. A similar unstable behavior is  
484 triggered by a decrease in blade pitch, in this case the platform swings backward, reducing apparent wind speed and rotor speed,  
485 promoting further blade pitch reductions. As explained in Sect. 3.3, controller gains were reduced to avoid this phenomenon (see  
486 (Larsen and Hanson, 2007) for a detailed explanation on the effectiveness of this strategy). Despite this, as confirmed by the  
487 increased platform pitch standard deviation in Fig. 3 and blade pitch standard deviation in Fig. 4, unstable behavior emerged at  
488 11 and 13 m/s wind speed. This can be seen clearly in Fig. 10, where the time series of platform pitch and blade pitch for the

489 three FOWT designs during a 13 m/s DLC 1.2 simulation are shown - and also in Fig 17 (d) later on in this study. In Fig. 10, the  
 490 OC4 model is not affected by pitch self-excitation, while the Hexafloat and Softwind models are. In the latter two models,  
 491 DeepLines is the least influenced by the phenomenon and QBlade is the most affected, despite all three codes using the same  
 492 controller.



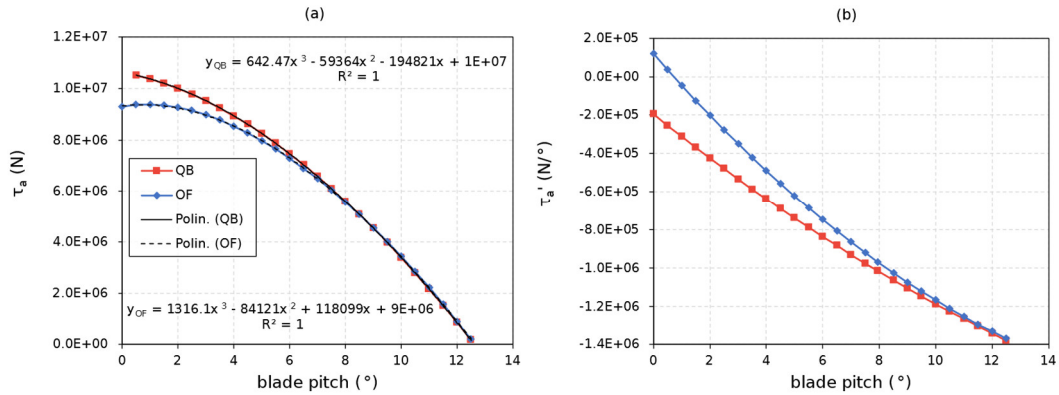
493  
 494 **Figure 10: Time series of blade pitch (top row) and platform pitch (bottom row) for a 13 m/s simulation in DLC 1.2. Softwind (a, b),**  
 495 **Hexafloat (c, d) and OC4 (e, f).**

496 Various physical phenomena could cause such a difference in excitation. However, by process of exclusion, differences in  
 497 hydrodynamic excitation are unlikely to be the cause of the increased self-excitation in QBlade, as nearly identical response  
 498 in QBlade and OpenFAST was noted at the Softwind’s pitch natural frequency in part one of this study ((Behrens De Luna et  
 499 al., 2023), Fig. 13). Moreover, the way unsteady aerodynamics are modelled is also not the cause, as switching to DBEM in  
 500 QBlade did not improve agreement in this regard with respect to OpenFAST (not shown herein for brevity). In addition, as  
 501 stated previously, OpenFAST does not include blade torsion. However, switching to a rigid structure did not improve the  
 502 agreement of OpenFAST and QBlade. A possible explanation for the difference in blade pitch - platform pitch self-excitation  
 503 was put forward in part one of this study (Behrens De Luna et al., 2023) and is related to increased aerodynamic torque  
 504 variation in QBlade with respect to the other two codes. Indeed, upon further investigations, differences in the system  
 505 dynamics, and how they interact with the control system, could explain the observed behavior. As explained in detail by Abbas  
 506 et al. (Abbas et al., 2022), the controller and turbine can be seen as a closed-loop second-order system, characterized by a  
 507 natural frequency at a certain operating wind speed:

$$508 \quad \omega^2 = k_i(U_{op})B = k_i(U_{op}) \frac{N_g \partial \tau_a}{J \partial \beta} \quad (1)$$

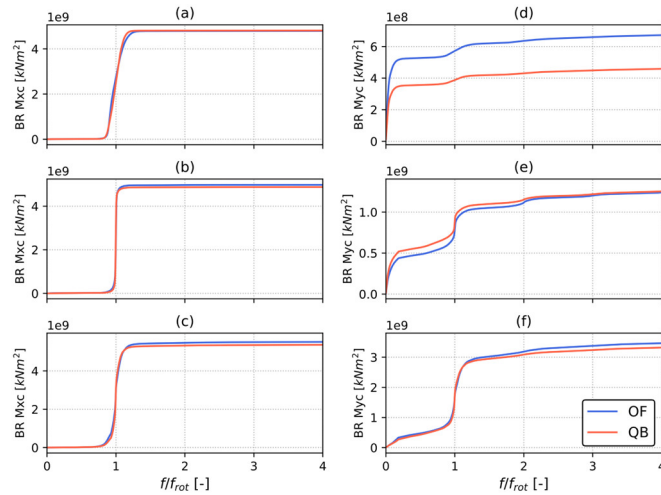
509 where  $N_g$  and  $J$  are the gearbox ratio and rotor inertia, which are the same in OpenFAST, QBlade and DeepLines. The higher  
 510 the natural frequency, the more responsive the system is to an external disturbance such as a platform pitch oscillation. The  
 511 integral controller gain  $k_i$  is also the same in the two codes, as it depends on the controller tuning. The slope of the aerodynamic  
 512 torque as a function of blade pitch is, however, different in the two codes. The derivative of aerodynamic torque as a function

513 of blade pitch for the mean 11 m/s operating conditions is shown in Fig. 11 (b). As  $\frac{\partial \tau_a}{\partial \beta}$  is larger in magnitude for QBlade at  
 514 the mean operating blade pitch of approximately  $0.5^\circ$ , from eq. 1,  $\omega^2$  is also larger, leading to increased self-excitation in  
 515 QBlade. This highlights how small differences in aerodynamics can lead to different controller response and influence turbine  
 516 load predictions significantly.



517  
 518 **Figure 11: (a) aerodynamic torque as a function of blade pitch for OpenFAST and QBlade for 11 m/s operating TSR,**  
 519 **and relative trendlines. (b) derivative of aerodynamic torque as a function of blade pitch computed from analytic**  
 520 **derivative of trendlines.**

521 Despite QBlade and OpenFAST lifetime DELs being very close, the OC4 FOWT design highlights some interesting behavior,  
 522 and differs in some key aspects from the Softwind FOWT design. CPSDs of blade root bending moments can, again, help  
 523 investigate the causes of the differences in Lifetime DELs and are shown for the in Figure 12. Focusing on out-of-plane root  
 524 bending moment (TB My), differences in 1P excitation that are highlighted for the Softwind design (Fig. 9) are not apparent in  
 525 OC4. The larger difference in 1P excitation between models on the Softwind design with respect to the OC4 design can likely  
 526 be explained by the size difference of the two rotors. As found by Madsen et al., (Madsen et al., 2020) non-uniform rotor loading  
 527 due to turbulence and wind shear increases with rotor size. For a larger rotor, a higher portion of the turbulent flow structures  
 528 feature a length scale that is smaller than the rotor diameter, shifting a higher ratio of the total energy in the turbulent spectrum  
 529 from lower frequencies to the 1P frequency and multiples. As for wind shear, a larger rotor operates in a larger portion of the  
 530 atmospheric boundary layer, meaning that each blade experiences more inflow variation during a revolution. As these  
 531 phenomena increase in magnitude they are expected to increase the differences between aerodynamic models at 1P frequency.

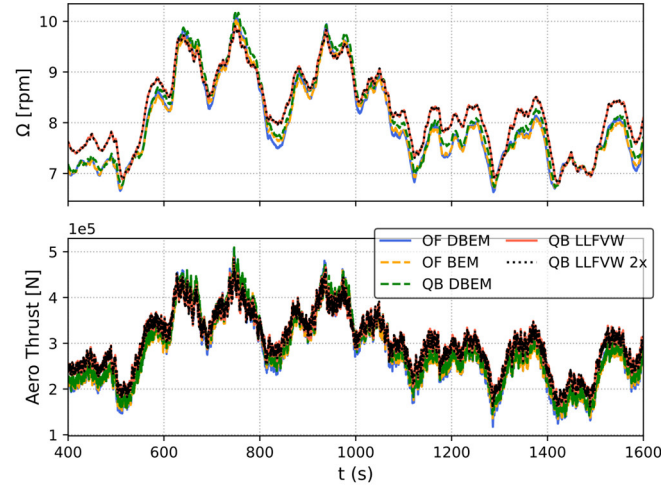


532

533

534

**Figure 12: Cumulative Power Spectral Density (CPSD) of blade root in-plane (a-c) and out-of-plane (d-f) bending moment for the OC4 model. PSD is computed on all simulations with 7 m/s (a, d), 13 m/s (b, e) and 23 m/s (c, f) mean wind speed.**



535

536

537

538

**Figure 13: Time series of rotor speed and aerodynamic thrust in a 7 m/s simulation of the OC4 test-case. Various wake models are compared; OpenFAST DBEM (Branlard et al., 2022), OpenFAST BEM (Ning et al., 2015), QBlade DBEM (Madsen et al., 2020) and QBlade LLFVW (Marten, 2020).**

539

540

541

542

543

544

545

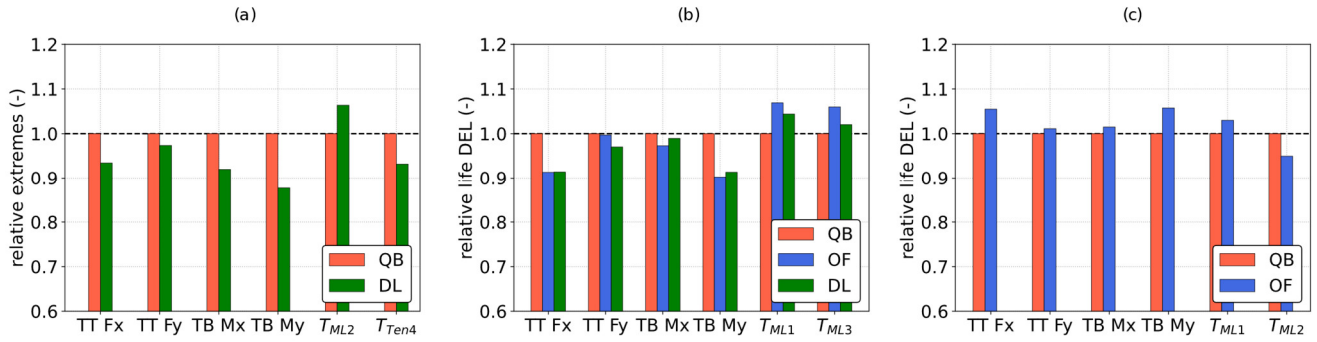
On the other hand, the low frequency excitation difference that was noted for the Softwind design is also found for the OC4 design (Fig. 12 (d)) and, although not shown herein for brevity, is also found to be one of the main drivers of the higher Lifetime DELs in OpenFAST (Fig. 8). To better understand this difference, additional simulations were carried out with additional aerodynamic models in both QBlade and OpenFAST in an attempt to isolate the cause of such differences. In particular, OpenFAST simulations were performed using quasi-steady BEM without dynamic induction corrections (OpenFAST BEM). QBlade on the other hand was run using LLFVW with doubled wake length (LLFVW x2) and with the polar-BEM method (Madsen et al., 2020) (QBlade DBEM). Time series of rotor speed and aerodynamic thrust are shown in Fig. 13 for a 7 m/s mean

546 wind speed simulation in DLC 1.2. As shown in Fig. 13, larger variations in rotor speed can be noted in the BEM-based models.  
547 This phenomenon is present in both QBlade and OpenFAST and no improvement with respect to QBlade LLFVW is noted when  
548 a dynamic induction correction is used. On the other hand, doubling the wake length in the LLFVW simulation has little to no  
549 effect on rotor speed, indicating that the wake cut-off length used in the study is adequate. The larger rotor speed variation in  
550 BEM models causes rotor thrust to vary more as TSR varies, thus causing the additional low-frequency loading shown in Fig.  
551 13.

552 These results can be put into perspective by comparing them to other authors' findings. Indeed, differences between BEM-based  
553 and LLFVW aerodynamic models in the prediction of blade root fatigue loads have also been noted by other authors. Boorsma  
554 et al. (Boorsma et al., 2020) attributed the differences observed at 1P frequency to different induction tracking of the BEM  
555 models during blade revolution, which causes differences in aerodynamic loading amplitude if wind shear, yaw misalignment,  
556 rotor tilt and, in the case of FOWTs, platform pitch are present. In addition to 1P differences, Perez-Becker et al. (Perez-Becker  
557 et al., 2020) also noted differences between LLFVW and BEM at low frequencies, the latter mainly being caused by different  
558 blade pitch actuation in the models. In the context of FOWTs, Corniglion (Corniglion, 2022) also found blade root fatigue loads  
559 predicted with a LLFVW model to be lower than those computed with a BEM-based aerodynamic tool. In this context, the higher  
560 fatigue loads that are noted in OpenFAST are in line with these findings. However, the same cannot be said for DeepLines that  
561 predicts lower lifetime DELs than the LLFVW-based QBlade.

#### 562 **4.3.1 Tower Base and Mooring Fatigue Loads**

563 Tower top, tower base and mooring lifetime DELs are shown in Fig. 14 for the three FOWT designs. The OC4 and Hexafloat  
564 designs show a similar trend to those shown in Fig. 8; lower lifetime DELs for DeepLines and higher Lifetime DELs for  
565 OpenFAST. Differently from blade root fatigue loads however, OpenFAST and DeepLines show good agreement in terms of  
566 lifetime DELs in Fig. 14 for the Softwind design. Tower-related fatigue loads are lower than QBlade, while mooring line fatigue  
567 predictions are higher. Moreover, differences in side-side tower loads (TT Fy and TB Mx) appear to be smaller than those found  
568 in the respective fore-aft sensors (TT Fx and TB My). These load sensors are arguably less influenced by aerodynamics, as the  
569 wind is always aligned with the global X direction, and more influenced by hydrodynamics, as wave headings range from -150°  
570 to 150°. In this context the good agreement in side-side loads is expected as hydrodynamics are modeled similarly in all three  
571 codes.



572

573

574

575

**Figure 14: Lifetime DELs normalized with respect to values computed in QBlade. Yaw bearing shear forces in p coordinate system and tower base fore-aft and side-side bending moments and shear forces in t coordinate system. From left to right: DTU 10MW Hexafloat, DTU 10MW Softwind and NREL 5MW OC4.**

576

577

The differences between the three models can be analyzed in more detail by comparing 1Hz DELs weighted by the probability of each environmental condition to occur:

578

$$\overline{DEL}_i = p_i * DEL = p_i \left( \frac{\sum_j n_j A_j^m}{t} \right)^{1/m} \quad (2)$$

579

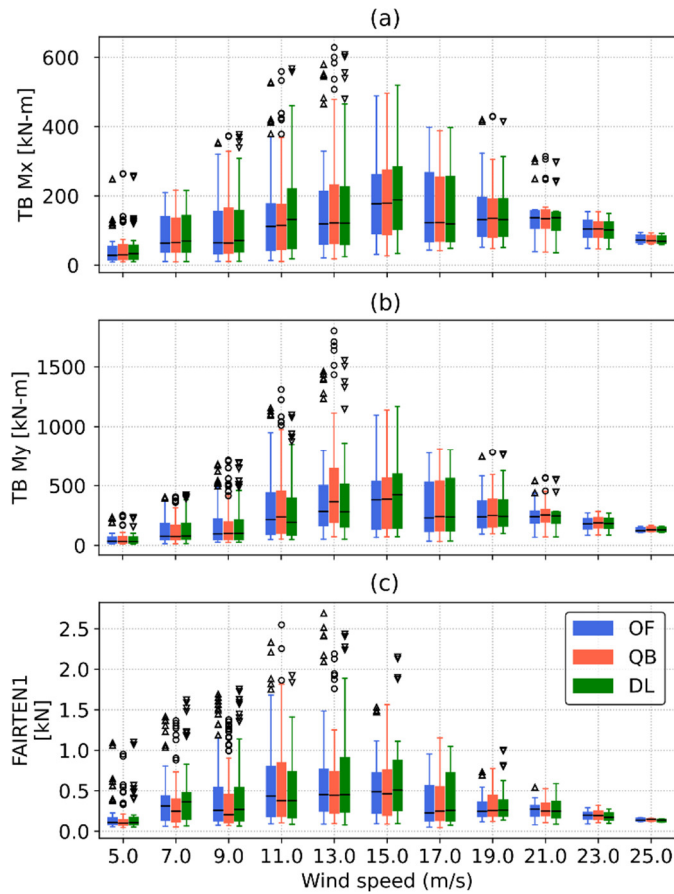
580

581

582

$p_i$  is the probability of each condition to occur,  $n_j$  and  $A_j$  are the combinations of rainflow counted j-th number of cycles and amplitude in each simulation and m is the Wöhler curve exponent, equal to 10 for the composite blades and 4 for the other steel components. As discussed in Sect. 2.4, 1Hz DELs multiplied by their respective probability of occurrence are representative of the contribution to lifetime fatigue loads of each operating condition.



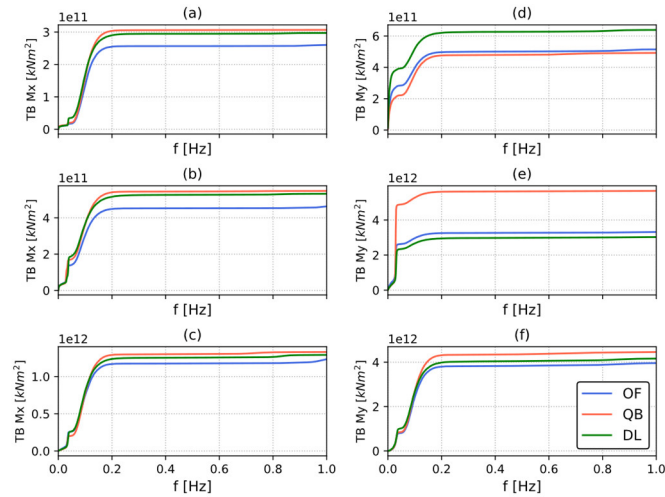


583

584 **Figure 15: Statistics of tower base bending moment and fairlead tension 1Hz zero-mean Damage Equivalent Loads weighted by the**  
 585 **probability of each environmental bin they refer to for the Softwind model. The boxes represent the 1<sup>st</sup> and 3<sup>rd</sup> quartiles, the whiskers**  
 586 **represent the data range and are found by adding/subtracting to the box edges 1.5 times the interquartile (IQR) range, the horizontal**  
 587 **line is the median of the data and flier values are shown as scatter points.**

588

589 Statistics of tower base and fairlead tension of one of the upwind mooring lines 1Hz DELs for the Softwind design are shown in  
 590 Fig. 15. From a fatigue damage standpoint, the most relevant wind speeds are included between 9 m/s and 19 m/s wind speed.  
 591 While 1Hz DELs are very close for all three numerical codes in Fig. 15 (a), the analysis of Fig. 15 (b) can help pinpoint the root  
 592 cause of the increased Lifetime DEL prediction in QBlade. In fact, while the three codes agree well across most wind speeds,  
 593 1Hz DELs are statistically higher for QBlade particularly in the 11 m/s and 13 m/s wind speed bins. The CPSDs of tower base  
 594 bending moments for the 7 m/s, 13 m/s and 23 m/s wind speed bins are shown in Figure 16. It stands out that tower base excitation  
 595 is dominated by low-frequency peaks, corresponding to the floater's natural surge/sway and pitch/roll natural frequencies, and  
 596 by response in the wave excitation frequency band. Moreover, contrary to blade root loads, 1P and 3P excitation is nearly  
 irrelevant as the CPSDs show a flat profile from 0.2 Hz and upwards.



597

598

599

**Figure 16: Cumulative Power Spectral Density (CPSD) of tower base side-side (a-c) and fore-aft (d-f) bending moment for the Softwind test-case. CPSD is computed on all simulations with 7 m/s (a, d), 13 m/s (b, e) and 23 m/s (c, f) mean wind speed.**

600

Regarding fore-aft bending moment (TB My), at 7 m/s (Fig. 16 (d)), low-frequency aerodynamic excitation is the main driver of differences between QBlade – that shows lower response and fatigue loads at this wind speed – and the BEM-based codes. These differences are caused by the higher rotor speed variations recorded in OpenFAST and especially in DeepLines, as minimum rotor speed is not enforced in this code. The higher rotor speed variation leads to higher variation in aerodynamic forcing, as shown in Fig. 13. This phenomenon also contributes to the higher platform pitch variation that is observed for the BEM based codes (Fig. 4), further increasing low-frequency TB My excitation.

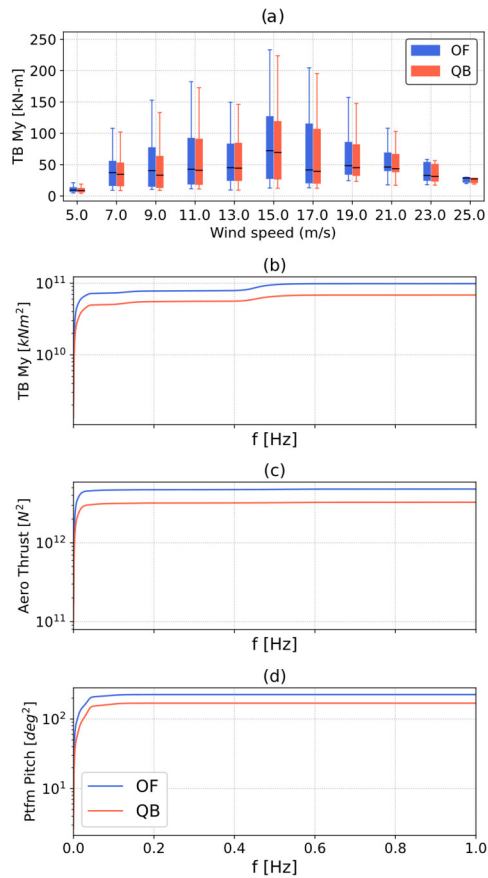
606

When analyzing Fig 16 (e), higher response at the floater pitch natural frequency is noted in QBlade. The cause of the increased response is floater-pitch blade-pitch instability, discussed in detail in Sect. 4.3.1

608

The same phenomenon also impacts the OC4 testcase, as shown in Fig. 17. The largest differences between OpenFAST and QBlade in the fore-aft tower base bending moment 1Hz DELs are located in the 9 m/s wind speed bin (Fig. 17 (a)). The CPSDs of aerodynamic thrust, platform pitch and TB My (Figs. 17 (b,c,d)) show that the main differences between the codes are found at very low frequencies, and are again caused by differences in aerodynamic response that are amplified by platform pitch and rotor speed variations.

612



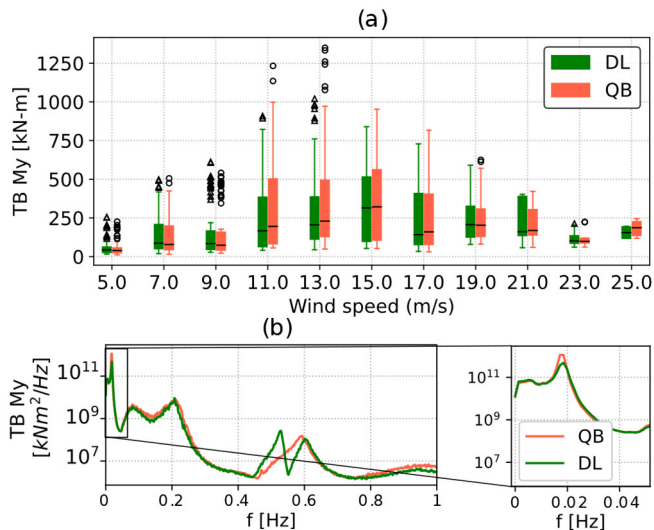
613

614 **Figure 17: (a) Statistics of tower base fore-aft bending moment 1Hz zero-mean Damage Equivalent Loads weighted by the probability**  
 615 **of each environmental bin they refer to for the OC4 model. The boxes represent the 1<sup>st</sup> and 3<sup>rd</sup> quartiles, the whiskers represent the**  
 616 **data range and are found by adding/subtracting to the box edges 1.5 times the interquartile (IQR) range, the horizontal line is the**  
 617 **median of the data and flier values are shown as scatter points. (b,c,d) Cumulative Power Spectral Density (CPSD) of tower base fore-**  
 618 **aft bending moment, aerodynamic thrust and platform pitch for the OC4 design. PSD is computed on all simulations with 9 m/s mean**  
 619 **wind speed.**

620 Going back to the Softwind FOWT concept, at 13 m/s (Fig. 16 (e)) the largest difference between QBlade and the other codes  
 621 is at the floater pitch natural frequency, where TB My PSD is much larger in the former code. The higher response is caused by  
 622 the same phenomenon that causes higher blade root CPSDs at 13 m/s wind speed in QBlade (Fig. 9): floater and blade pitch self-  
 623 excitation. In the case of tower base loads, in addition to cyclic variation in aerodynamic loads, cyclic inertial and gravitational  
 624 forcing become relevant load sources, as the weight of the tower itself and the Rotor Nacelle Assembly (RNA) are considerable.  
 625 Therefore, despite QBlade comparing well to the other two codes at other wind speeds (Fig. 16 (f)), the difference highlighted  
 626 at 13 m/s (Fig. 16 (e)) ultimately leads to higher TB My lifetime DELs for QBlade (Fig. 14).

627 As shown in Fig. 18, floater and blade pitch self-excitation also influence fatigue load predictions for the Hexafloat model. As  
 628 discussed previously, DeepLines predicts lower lifetime DELs than QBlade for this test-case. Contrary to floater-pitch-frequency

629 excitation, the peak in TB My response in correspondence of the tower first fore-aft natural frequency located at 0.2 Hz is  
 630 captured well by both DeepLines and QBlade (Fig. 18 (b,c)).



631  
 632 **Figure 18: (a) Statistics of fore-aft tower base bending moment 1Hz zero-mean Damage Equivalent Loads weighted by the probability**  
 633 **of each environmental bin they refer to for the Hexafloat model. The boxes represent the 1<sup>st</sup> and 3<sup>rd</sup> quartiles, the whiskers represent**  
 634 **the data range and are found by adding/subtracting to the box edges 1.5 times the interquartile (IQR) range, the horizontal line is the**  
 635 **median of the data and flier values are shown as scatter points. (b) Power Spectral Density (PSD) of tower base fore-aft bending**  
 636 **moment for the Hexafloat test-case. PSD is computed on all simulations with 11 m/s mean wind speed.**

## 637 5 Conclusions

638 An extensive code-to-code comparison with realistic environmental conditions is performed in this study. Three floating wind  
 639 turbine substructure designs, a semi-submersible, a spar-buoy and the Hexafloat concept proposed by Saipem are compared in  
 640 multiple environmental conditions involving hundreds of simulations. The considered codes include TU Berlin's QBlade,  
 641 NREL's OpenFAST and Principia's DeepLines. Statistics, extreme and fatigue loads of key load sensors are discussed.  
 642 OpenFAST and QBlade results were refined over the span of several months, correcting small bugs that may arise in such a  
 643 complex set-up and ultimately aligning the models better. DeepLines has not benefitted from such improvements due to budget  
 644 and time limitations, which explains the poorer agreement noted for this code in many instances. These results are nevertheless  
 645 included as they are representative of what could be achieved with limited time and budget often connected to industrial  
 646 processes.

647 The statistical comparison revealed good agreement between the codes in their ability to predict general system dynamics.  
 648 Nonetheless some differences, particularly in the coupling with the controller, emerged. Blade pitch – floater pitch self-excitation  
 649 is noted in the Softwind and Hexafloat designs. While this phenomenon is present in all three codes, it is more accentuated in  
 650 QBlade, despite all three sharing the blade pitch controller logic. A possible explanation for this phenomenon was put forward  
 651 by the authors in a twin study (Behrens De Luna et al., 2023) and is linked to larger variations in rotor speed in QBlade. Above

652 rated wind speed, such variations cause the pitch controller to intervene more aggressively, thus triggering the floater pitch  
653 instability. Upon further investigation, aerodynamic torque is found to be more sensitive to blade pitch variations at low wind  
654 speeds in QBlade, which causes the response of the coupled turbine and controller system to be faster and thus more prone to  
655 instability. This self-excitation is found to be the cause of increased fore-aft tower base and out-of-plane root bending moment  
656 lifetime DELs in QBlade in both the Hexafloat and Softwind designs and demonstrated how small differences in modeling can  
657 have a significant impact on design loads. No clear trend is noted when ultimate loads are compared. Taking QBlade as a  
658 reference point, ultimate loads are regularly found to be in the  $\pm 15\%$  range, with only some exceeding it. The compared ultimate  
659 loads are selected according to the so-called “mean of max” method according to international standard indications (IEC61400-  
660 1, Annex G). As demonstrated in this work, small differences in ultimate loads may cause the method to select a different  
661 maximum, amplifying the difference between the models. In addition, the different FOWT designs have a different dynamical  
662 response to the environmental conditions, thus affecting the ultimate loads differently.

663 Fatigue loads, namely lifetime DELs, show a clear trend: OpenFAST generally predicts higher loads than QBlade, while  
664 DeepLines predicts lower lifetime fatigue loads. The reason for the latter being a different model set-up of the Softwind design  
665 in DeepLines and the lower effect of the blade pitch-platform pitch instability in the Hexafloat design. The exception to this is  
666 represented by tower base lifetime DELs, which for the Softwind design, are lower in OpenFAST. The root cause of this behavior  
667 in the Softwind design is again the floater pitch – blade pitch interaction, which is higher in QBlade compared to the two other  
668 codes. The higher DELs in OpenFAST are in line with other authors’ findings, who observed higher fatigue loads in BEM-based  
669 codes compared to in LLFVW-based codes. In this study however, OpenFAST differs from the other two codes also in the  
670 structural modeling: the former utilizing a modal structural model without the ability to model blade torsion while the latter two  
671 feature a multi-body model that includes blade torsion. Despite the trend being consistent between the codes, the magnitude of  
672 the lifetime DEL overestimation is different in the two designs where OpenFAST and QBlade are compared, OC4 and Softwind.  
673 In fact, in Softwind, blade root DELs are 2% to 14% higher in OpenFAST, while in OC4 they are up to 1.5% higher. The  
674 analysis of CPSDs highlighted greater response at the 1P frequency in OpenFAST in the latter design, while in OC4 the main  
675 difference between OpenFAST and QBlade is mostly confined to higher response in OpenFAST at very low frequencies. This  
676 low frequency difference is driven by increased rotor speed variation, in turn caused by differences in aerodynamic modeling.  
677 In conclusion, the relatively simpler model assumptions adopted in OpenFAST are found to be able to reproduce the system  
678 dynamics adequately for the considered designs. No clear trend is noted for extreme loads.. In fact, differences between the  
679 codes are mostly in the  $\pm 10\%$  range, but deviations exceeding 20% were observed in some cases. Moreover, these differences  
680 could not be traced back to a specific engineering model or modelling choice. In this regard, including a larger set of extreme  
681 load cases with more parameter variations could help give a clearer picture of the differences in ultimate loading between the  
682 codes and the FOWT designs. On the other hand, a clear trend is noted in fatigue loads. This may be explained by the difference  
683 in aerodynamic models, in particular the comparison between the BEM-based OpenFAST and the LLFVW-based QBlade is  
684 consistent with existing scientific literature. DeepLines however contradicts this trend. While this may be, at least in part, due to  
685 setup differences in the Softwind design and to this code being less prone to blade pitch-floater pitch self-excitation, this aspect

686 is identified as a key point for future research. Overall, the differences between the compared modelling theories are consistent  
687 with the existing body of literature on onshore wind turbines. The greater movement that FOWTs are allowed did not exacerbate  
688 the differences to the point that simpler models, such as OpenFAST, are outdated. This study has shown that, within the  
689 limitations highlighted in this and other similar works, these models are still relevant for industry and for many research  
690 applications.

691

## 692 **Nomenclature**

693	COD	Co-Directional
694	CPSD	Cumulative Power Spectral Density
695	CS	Coordinate System
696	DLC	Design Load Case
697	$E[\varepsilon_1   \varepsilon_2]$	Expected value of $\varepsilon_1$ conditioned on $\varepsilon_2$
698	ECD	Extreme Change of Direction with coherent gust
699	ESS	Extreme Sea State
700	ETM	Extreme Turbulence Model
701	EWM	Extreme Wind Model
702	FOWT	Floating Offshore Wind Turbine
703	MUL	Multi-Directional
704	NSS	Normal Sea State
705	NTM	Normal Turbulence Model
706	OC4	OC4 DeepCWind semi-submersible
707	PSD	Power Spectral Density
708	SSS	Severe Sea State
709	$H_s$	Significant Wave Height (m)
710	$T_p$	Peak Spectral Period (s)
711	$M_{WW}$	Mean Wind-Wave misalignment ( $^\circ$ )
712	$U_w$	Wind Speed
713	$V_{in}/V_{out}$	Cut-in/Cut-out wind speed (m/s)

714



**Funding** This work has received support from the FLOATECH project, funded by the European Union's Horizon 2020 research and innovation programme under grant agreement No. 101007142

717

718 **Data Availability** The simulation results used in this study are publicly available at [10.5281/zenodo.7254241](https://doi.org/10.5281/zenodo.7254241). The met-ocean  
719 conditions are also available at [doi.org/10.1088/1742-6596/2385/1/012117](https://doi.org/10.1088/1742-6596/2385/1/012117). The QBlade-Ocean models upon which the models

720 tested herein are based are available at 10.5281/zenodo.6397352 (OC5), 10.5281/zenodo.6397358 (Softwind),  
721 10.5281/zenodo.6397313 (Hexafloat) and the modifications required to align them with the models tested herein are detailed in  
722 10.5281/zenodo.7817707.

723

724 **Competing Interest** At least one of the (co-)authors is a member of the editorial board of Wind Energy Science. The peer-  
725 review process was guided by an independent editor, and the authors also have no other competing interests to declare.

## 726 **References**

727 Abbas, N. J., Zalkind, D. S., Pao, L., and Wright, A.: A reference open-source controller for fixed and floating offshore wind  
728 turbines, *Wind Energy Science*, 7, 53–73, <https://doi.org/10.5194/wes-7-53-2022>, 2022.

729 IEC TS 61400-3-2:2019 | IEC Webstore: <https://webstore.iec.ch/publication/29244>, last access: 3 January 2023.

730 Antonia Krieger, Gireesh K. V. Ramachandran, Luca Vita, Pablo Gómez Alonso, Gonzalo Gónzales Almeria, Joannès Barque,  
731 and Goren Aguirre: D7.2 LIFEs50+ Design Basis, 2015.

732 Arnal, V.: Experimental modelling of a floating wind turbine using a “software-in-the-loop” approach, These de doctorat,  
733 Ecole centrale de Nantes, 2020.

734 Bak, C., Zahle, F., Bitsche, R., Taeseong, K., Anders, Y., Henriksen, L. C., Natarajan, A., and Hansen, M. H.: Description of  
735 the DTU 10MW Reference Wind Turbine, DTU Wind Energy, Roskilde, Denmark, 2013.

736 Behrens De Luna, R., Perez-Becker, S., Saverin, J., Marten, D., Papi, F., Ducasse, M.-L., Bonnefoy, F., Bianchini, A., Nayeri,  
737 C. N., and Paschereit, C. O.: Verifying QBlade-Ocean: A Hydrodynamic Extension to the Wind Turbine Simulation Tool  
738 QBlade, *Wind Energy Science Discussions*, 1–36, <https://doi.org/10.5194/wes-2023-117>, 2023.

739 Bergua, R. and et. al.: OC6 Project Phase III: Validation of the Aerodynamic Loading on a Wind Turbine Rotor Undergoing  
740 Large Motion Caused by a Floating Support Structure, *Wind Energy Science Journal*, 8, 465–485, <https://doi.org/10.5194/wes-8-465-2023>, 2023.

742 Boorsma, K., Wenz, F., Lindenburg, K., Aman, M., and Kloosterman, M.: Validation and accommodation of vortex wake  
743 codes for wind turbine design load calculations, *Wind Energ. Sci.*, 5, 699–719, <https://doi.org/10.5194/wes-5-699-2020>, 2020.

744 Borg, M.: LIFES50+ Deliverable D1.2: Wind turbine models for the design, DTU Wind Energy, Risø, Denmark, 2015.

745 Branlard, E., Jonkman, B., Pirrung, G. R., Dixon, K., and Jonkman, J.: Dynamic inflow and unsteady aerodynamics models  
746 for modal and stability analyses in OpenFAST, *J. Phys.: Conf. Ser.*, 2265, 032044, <https://doi.org/10.1088/1742-6596/2265/3/032044>, 2022.

748 Buhl, M.: MExtremes User’s Guide, 9, 2015.

749 Burton, T. (Ed.): *Wind energy: handbook*, J. Wiley, Chichester ; New York, 617 pp., 2001.

750 Cornignon, R.: aero-elastic modeling of floating wind turbines with vortex methods, PhD Thesis, École des Ponts ParisTech,  
751 2022.

752 DNVGL: DNVGL-ST-0437 - Loads and site conditions for wind tubines, DNVGL AS, 2016.

- 753 DNVGL: DNVGL-ST-0119 - Floating wind turbine structures, DNVGL AS, 2018.
- 754 Faltinsen, O.: Sea Loads on Ships and Offshore Structures, Cambridge University Press, 1993.
- 755 Hansen, M. O. L.: Aerodynamics of wind turbines, 2nd ed., Earthscan, London ; Sterling, VA, 181 pp., 2008.
- 756 Haselsteiner, A. F., Lehmkuhl, J., Pape, T., Windmeier, K.-L., and Thoben, K.-D.: ViroCon: A software to compute  
757 multivariate extremes using the environmental contour method, *SoftwareX*, 9, 95–101,  
758 <https://doi.org/10.1016/j.softx.2019.01.003>, 2019.
- 759 Haselsteiner, A. F., Sander, A., Ohlendorf, J.-H., and Thoben, K.-D.: Global Hierarchical Models for Wind and Wave  
760 Contours: Physical Interpretations of the Dependence Functions, in: Volume 2A: Structures, Safety, and Reliability, ASME  
761 2020 39th International Conference on Ocean, Offshore and Arctic Engineering, Virtual, Online, V02AT02A047,  
762 <https://doi.org/10.1115/OMAE2020-18668>, 2020.
- 763 Haselsteiner, A. F., Coe, R. G., Manuel, L., Chai, W., Leira, B., Clarindo, G., Guedes Soares, C., Hannesdóttir, Á., Dimitrov,  
764 N., Sander, A., Ohlendorf, J.-H., Thoben, K.-D., Hauteclouque, G. de, Mackay, E., Jonathan, P., Qiao, C., Myers, A., Rode,  
765 A., Hildebrandt, A., Schmidt, B., Vanem, E., and Huseby, A. B.: A benchmarking exercise for environmental contours, *Ocean  
766 Engineering*, 236, 109504, <https://doi.org/10.1016/j.oceaneng.2021.109504>, 2021.
- 767 Hayman, G. J.: MLife Theory Manual for Version 1.00, NREL, 2012.
- 768 International Electrotechnical Commission: TS 61400-3-1, Wind energy generation systems - Part 3-1: Design requirements  
769 for fixed offshore wind turbines, 2019.
- 770 Jonkman, B. J.: TurbSim User's Guide v2.00.00, Renewable Energy, 2014.
- 771 Jonkman, J.: Definition of the Floating System for Phase IV of OC3, <https://doi.org/10.2172/979456>, 2010.
- 772 Jonkman, J. and Musial, W.: Offshore Code Comparison Collaboration (OC3) for IEA Task 23 Offshore Wind Technology  
773 and Deployment, *Renewable Energy*, 74, 2010.
- 774 Jonkman, J., Butterfield, S., Musial, W., and Scott, G.: Definition of a 5-MW Reference Wind Turbine for Offshore System  
775 Development, <https://doi.org/10.2172/947422>, 2009.
- 776 Jonkman, J. M. and Matha, D.: Dynamics of offshore floating wind turbines-analysis of three concepts, *Wind Energ.*, 14, 557–  
777 569, <https://doi.org/10.1002/we.442>, 2011.
- 778 Kurnia, R., Ducrozet, G., and Gilloteaux, J.-C.: Second Order Difference- and Sum-Frequency Wave Loads in the Open-  
779 Source Potential Flow Solver NEMOH, ASME 2022 41st International Conference on Ocean, Offshore and Arctic  
780 Engineering, <https://doi.org/10.1115/OMAE2022-79163>, 2022.
- 781 Larsen, T. J. and Hanson, T. D.: A method to avoid negative damped low frequent tower vibrations for a floating, pitch  
782 controlled wind turbine, *J. Phys.: Conf. Ser.*, 75, 012073, <https://doi.org/10.1088/1742-6596/75/1/012073>, 2007.
- 783 Le Cunff, C., Heurtier, J.-M., Piriou, L., Berhault, C., Perdrizet, T., Teixeira, D., Ferrer, G., and Gilloteaux, J.-C.: Fully  
784 Coupled Floating Wind Turbine Simulator Based on Nonlinear Finite Element Method: Part I — Methodology, in: Volume 8:  
785 Ocean Renewable Energy, ASME 2013 32nd International Conference on Ocean, Offshore and Arctic Engineering, Nantes,  
786 France, V008T09A050, <https://doi.org/10.1115/OMAE2013-10780>, 2013.



- 787 Lenfest, E., Goupee, A. J., Wright, A., and Abbas, N.: Tuning of Nacelle Feedback Gains for Floating Wind Turbine  
788 Controllers Using a Two-DOF Model, in: Volume 9: Ocean Renewable Energy, ASME 2020 39th International Conference  
789 on Ocean, Offshore and Arctic Engineering, Virtual, Online, V009T09A063, <https://doi.org/10.1115/OMAE2020-18770>,  
790 2020.
- 791 Madsen, H. A., Larsen, T. J., Pirrung, G. R., Li, A., and Zahle, F.: Implementation of the blade element momentum model on  
792 a polar grid and its aeroelastic load impact, *Wind Energy Science*, 5, 1–27, <https://doi.org/10.5194/wes-5-1-2020>, 2020.
- 793 Marten, D.: QBlade: a modern tool for the aeroelastic simulation of wind turbines, 2020.
- 794 Marten, D., Lennie, M., Pechlivanoglou, G., Nayeri, C. N., and Paschereit, C. O.: Implementation, optimization and validation  
795 of a nonlinear lifting line free vortex wake module within the wind turbine simulation code qblade, *Proceedings of the ASME  
796 Turbo Expo*, <https://doi.org/10.1115/GT2015-43265>, 2015.
- 797 Ning, A., Hayman, G., Damiani, R., and Jonkman, J. M.: Development and Validation of a New Blade Element Momentum  
798 Skewed-Wake Model within AeroDyn, in: 33rd Wind Energy Symposium, 33rd Wind Energy Symposium, Kissimmee,  
799 Florida, <https://doi.org/10.2514/6.2015-0215>, 2015.
- 800 Papi, F. and Bianchini, A.: Technical challenges in floating offshore wind turbine upscaling: A critical analysis based on the  
801 NREL 5 MW and IEA 15 MW Reference Turbines, *Renewable and Sustainable Energy Reviews*, 162, 112489,  
802 <https://doi.org/10.1016/j.rser.2022.112489>, 2022.
- 803 Papi, F. and Bianchini, A.: Annotated Guidelines for the Simulation of Floating Offshore Wind Turbines in a Real  
804 Environment, in: *Proceedings of OMAE 2023*, OMAE 2023, Melbourne, Australia, 2023.
- 805 Papi, F., Behrens De Luna, R., Saverin, J., Marten, D., Combreau, C., Troise, G., Mirra, G., and Bianchini, A.: D2.3. Design  
806 Load Case Database for Code-to-Code Comparison, 2022a.
- 807 Papi, F., Bianchini, A., Troise, G., Mirra, G., Marten, D., Saverin, J., Behrens De Luna, R., Ducasse, M.-L., and Honnet, J.:  
808 D2.4. Full report on the estimated reduction of uncertainty in comparison to the state-of-the-art codes OpenFAST and  
809 DeepLines Wind<sup>TM</sup>, FLOATECH, 2022b.
- 810 Papi, F., Perignon, Y., and Bianchini, A.: Derivation of Met-Ocean Conditions for the Simulation of Floating Wind Turbines:  
811 a European case study, *J. Phys.: Conf. Ser.*, 2385, 012117, <https://doi.org/10.1088/1742-6596/2385/1/012117>, 2022c.
- 812 Papi, F., Bianchini, A., Troise, G., Mirra, G., Marten, D., Saverin, J., Behrens de Luna, R., Ducasse, M.-L., and Honnet, J.:  
813 Deliverable 2.4 Full report on the estimated reduction of uncertainty in comparison to the state-of-the-art codes OpenFAST  
814 and DeepLines Wind, 2023.
- 815 Perez-Becker, S., Papi, F., Saverin, J., Marten, D., Bianchini, A., and Paschereit, C. O.: Is the Blade Element Momentum  
816 theory overestimating wind turbine loads? – An aeroelastic comparison between OpenFAST’s AeroDyn and QBlade’s Lifting-  
817 Line Free Vortex Wake method, *Wind Energ. Sci.*, 5, 721–743, <https://doi.org/10.5194/wes-5-721-2020>, 2020.
- 818 Perez-Becker, S., Saverin, J., Behrens de Luna, R., Papi, F., Combreau, C., Ducasse, M.-L., Marten, D., and Bianchini, A.:  
819 Deliverable 2.2 - Validation Report of QBlade-Ocean, 2022.
- 820 Robertson, A. and Jonkman, J.: Loads Analysis of Several Offshore Floating Wind Turbine Concepts, *International Society of  
821 Offshore and Polar Engineers 2011 Conference*, Maui, Hawaii, 10, 2011.

- 822 Robertson, A., Jonkman, J., Masciola, M., Song, H., Goupee, A., Coulling, A., and Luan, C.: Definition of the Semisubmersible  
823 Floating System for Phase II of OC4, <https://doi.org/10.2172/1155123>, 2014a.
- 824 Robertson, A., Jonkman, J., Vorpahl, F., Popko, W., Qvist, J., Frøynd, L., Chen, X., Azcona, J., Uzunoglu, E., Guedes Soares,  
825 C., Luan, C., Yutong, H., Pengcheng, F., Yde, A., Larsen, T., Nichols, J., Buils, R., Lei, L., Nygaard, T. A., Manolas, D.,  
826 Heege, A., Vatne, S. R., Ormberg, H., Duarte, T., Godreau, C., Hansen, H. F., Nielsen, A. W., Riber, H., Le Cunff, C., Beyer,  
827 F., Yamaguchi, A., Jung, K. J., Shin, H., Shi, W., Park, H., Alves, M., and Guérinel, M.: Offshore Code Comparison  
828 Collaboration Continuation Within IEA Wind Task 30: Phase II Results Regarding a Floating Semisubmersible Wind System,  
829 in: Volume 9B: Ocean Renewable Energy, ASME 2014 33rd International Conference on Ocean, Offshore and Arctic  
830 Engineering, San Francisco, California, USA, V09BT09A012, <https://doi.org/10.1115/OMAE2014-24040>, 2014b.
- 831 Robertson, A. N., Wendt, F., Jonkman, J. M., Popko, W., Dagher, H., Gueydon, S., Qvist, J., Vittori, F., Azcona, J., Uzunoglu,  
832 E., Soares, C. G., Harries, R., Yde, A., Galinos, C., Hermans, K., de Vaal, J. B., Bozonnet, P., Bouy, L., Bayati, I., Bergua, R.,  
833 Galvan, J., Mendikoa, I., Sanchez, C. B., Shin, H., Oh, S., Molins, C., and Debruyne, Y.: OC5 Project Phase II: Validation of  
834 Global Loads of the DeepCwind Floating Semisubmersible Wind Turbine, *Energy Procedia*, 137, 38–57,  
835 <https://doi.org/10.1016/j.egypro.2017.10.333>, 2017.
- 836 Robertson, A. N., Gueydon, S., Bachynski, E., Wang, L., Jonkman, J., Alarcón, D., Amet, E., Beardsell, A., Bonnet, P., Boudet,  
837 B., Brun, C., Chen, Z., Féron, M., Forbush, D., Galinos, C., Galvan, J., Gilbert, P., Gómez, J., Harnois, V., Haudin, F., Hu, Z.,  
838 Dreff, J. L., Leimeister, M., Lemmer, F., Li, H., Mckinnon, G., Mendikoa, I., Moghtadaei, A., Netzband, S., Oh, S., Pegalajar-  
839 Jurado, A., Nguyen, M. Q., Ruehl, K., Schünemann, P., Shi, W., Shin, H., Si, Y., Surmont, F., Trubat, P., Qvist, J., and  
840 Wohlfahrt-Laymann, S.: OC6 Phase I: Investigating the underprediction of low-frequency hydrodynamic loads and responses  
841 of a floating wind turbine, *J. Phys.: Conf. Ser.*, 1618, 032033, <https://doi.org/10.1088/1742-6596/1618/3/032033>, 2020.
- 842 Stewart, G. M.: Design Load Analysis of Two Floating Offshore Wind Turbine Concepts, University of Massachusetts  
843 Amherst, <https://doi.org/10.7275/7627466.0>, 2016.
- 844 Valamanesh, V., Myers, A. T., and Arwade, S. R.: Multivariate analysis of extreme metocean conditions for offshore wind  
845 turbines, *Structural Safety*, 55, 60–69, <https://doi.org/10.1016/j.strusafe.2015.03.002>, 2015.
- 846 Van Garrel, A.: Development of a wind turbine aerodynamics simulation module, 2003.
- 847 Vigara, F., Cerdán, L., Durán, R., Muñoz, S., Lynch, M., Doole, S., Molins, C., Trubat, P., and Gunache, R.: COREWIND  
848 D1.2 Design Basis, , <https://doi.org/10.5281/zenodo.4518828>, 2020.
- 849 Wang, L., Robertson, A., Jonkman, J., and Yu, Y.-H.: OC6 phase I: Improvements to the OpenFAST predictions of nonlinear,  
850 low-frequency responses of a floating offshore wind turbine platform, *Renewable Energy*, 187,  
851 <https://doi.org/10.1016/j.renene.2022.01.053>, 2022.
- 852 Yu, W.: D4.2 Public Definition of the Two LIFES50+ 10MW Floater Concepts, 32, n.d.

853

854

855

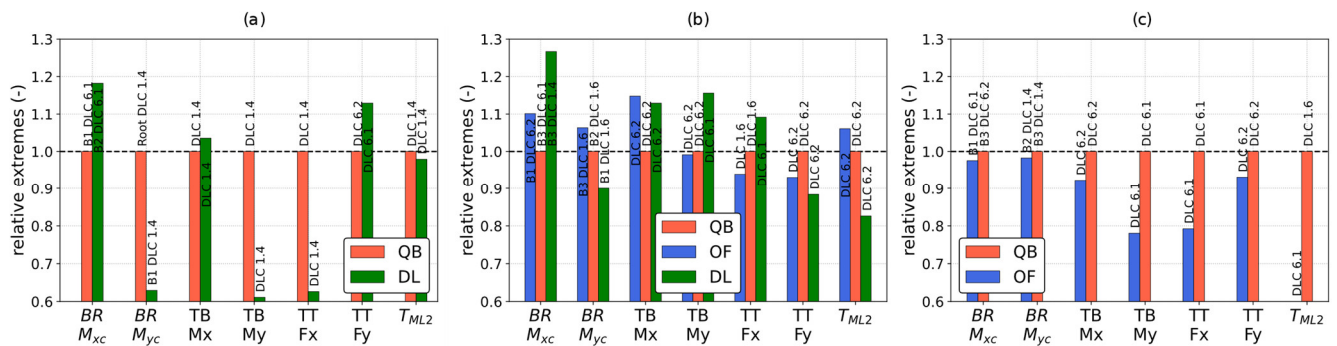
856

857

858  
859  
860  
861  
862  
863  
864  
865  
866  
867  
868  
869  
870  
871  
872

873 **6 Appendix A – Minimum Ultimate Loads**

874



875

876

877

**Figure A1: Selection of ultimate loads (minimum) recorded in the three simulation codes. (a) DTU 10MW Hexafloat, (b) DTU 10MW Softwind and (c) NREL 5MW OC4.**

